The Dynamics of Ice-Water Interfaces: Experimental and Numerical Investigation of Ice Scallops

by

© Victor Anyidoho

A Thesis submitted to the School of Graduate Studies in partial fulfillment of the

requirements for the degree of

Master of Engineering

Faculty of Engineering and Applied Science

Memorial University of Newfoundland

November 2023

St. John's Newfoundland and Labrador

Abstract

Floating glacial ice features, such as icebergs and ice islands may develop naturally textured ice surfaces due to melt processes, which can lead to the formation of local surface undulations commonly referred to as scallops. The mechanism for the formation of ice scallops was investigated using experimental and numerical techniques to help understand how these features are formed in nature. The variables investigated include temperature, scallop wavelength, and scallop geometry. A series of tests were conducted in a recirculation flume under specific experimental conditions at Reynolds numbers 23265, 30147, and 32768. Each test experiment was run for 10 minutes and observed for scallop formation. The experimental time frame was extended to 20 minutes to see if any additional scallops would be formed. Numerical simulation was conducted to complement the experimental results using commercial software. In both experimental and numerical investigations, the results showed a dominance of a visible recirculation region at the leading edge of the ice. The experimental results showed an increased ice melt rate when the approach fluid velocity was increased. Scallops were formed due to turbulence flow structures and spontaneous separation and reattachment of flow at the leading edge, giving rise to non-uniform melting at the ice-water interfaces. Three main phases of scallop development were identified: an initial flat ice geometry, a fully developed scallop, and an adjusting or evolving scallop. Due to the three-dimensional nature of the flow, portions of the water were directed to the lateral side of the ice, which led to a differential melt. The experimental results also showed a significant melting at the ice front or the leading edge of the ice. This is partly attributed to stagnation and pressure fluctuation within the recirculation bubble. The basal melt profile of the ice was measured using a contour gauge after each experimental run. The dynamic interaction of the water and ice interface resulted in shearing on the ice surface. The average basal melting was estimated at 40 mm relative to the initial origin of the ice. The frontal melt varied from 30 mm to 50 mm when the Reynolds number was increased.

The surface of the ice closest to the middle of the channel experienced a higher melt rate than other bottom surfaces of the scalloped ice since the maximum velocity occurs at the center of the channel. Scallops were observed to be formed due to fluid recirculation within the scalloped region, resulting in the evolving scallop geometry. A test to investigate the effect of Reynolds number on scallop wavelength showed a wavelength of 266 mm for Re = 32768, while no wavelength was observed for Re = 23265 and 30147. From the results, a partial feature was observed at the tail end of the ice for Re = 30147 but could not be classified as a full scallop. The measured temperature data indicated increased melting with an increasing Reynolds number. The temperature recorded for each thermocouple channel is observed to reduce from the leading edge to the tail end of the ice. Data from the numerical simulation showed fluid separation at the leading edge of the ice and subsequent reattachment of the fluid, which corroborates the non-uniform melting of the ice observed experimentally.

Acknowledgment

I want to express my profound gratitude to my supervisors, Dr. Rocky Taylor and Dr. Baafour Nyantekyi-Kwakye, for their consistent support, guidance, and motivation throughout my research. I am grateful for their technical, key contributions in fluid mechanics and heat transfer, ice mechanics, computational fluid dynamics, project management, statistical and data organization, and computation.

My appreciation also goes to all technical support from the fluid laboratory technicians for their help in instrumentation, sample preparation stages, and safety briefings. The model and fabrication lab's contribution cannot be overlooked, and I am grateful for your contribution during the early stages of model validation, feasibility discussions, and fabrication. I would love to show my most profound appreciation to C-CORE for providing the environment and helping with machinery during the sample-making process.

A special appreciation to funding providers, Memorial University of Newfoundland and Labrador, the Research Development Corporation of Newfoundland and Labrador (RDC), and Hibernia Management and Development Company, Ltd as well as NSERC.

Finally, I thank my family and other research team members for their emotional support.

Table of Contents

List of Figures

List of Tables

List of Abbreviations and Symbols

RANS	Reynolds Average Navier Stokes
LES	Large-Eddy Simulation
DNS	Direct Numerical Simulation
k-ε	Turbulence Kinetic-dissipation rate Model
k-ω	Turbulence Kinetic-specific dissipation rate Model
rms	Root Mean Square
ADCP	Acoustic Doppler Current Profiler
LDV	Laser Doppler Velocimetry
Hpz	High-Pressure Zone
Lpz	Low-Pressure Zone
PDE	Partial Differential Equations
NS	Navier–Stokes
SST	Shear Stress Transport
Re	Reynolds Number
t	Time
hs	Sensible Heat
h	Heat Transfer Coefficient
h_{reff}	Reference Enthalpy of the Material
T_{reff}	Reference Temperature
ρ	Density
H	Enthalpy
S	Source Term

$\tilde{E}$	Thermal Expansion Coefficient
μ	Dynamic Viscosity
VOF	Volume of Fluid
AL_O	Nominal / Local Area
AL_S	Local Area of Scalloped Ice Surface
c_p	Specific Heat
k	Turbulence Kinetic Energy
C_k	Kolmogorov’s Constant
ε	Turbulence Dissipation
κ	Von Kάrmάn Constant
Sd	Spatial Distance
Tc	Thermocouple Channel
U_i	Instantaneous fluid velocity
q'''	Volumetric rate of heat generation
$\dot{m}_{no}$	Mass transfer between two phases
I	Turbulence Intensity
ν	Kinematic viscosity
u'	Fluctuating velocity
μ_t	Turbulence viscosity
K	Coefficient of thermal conductivity
Ķ	Permeability of medium

Chapter 1: Introduction

1.1 Overview

Offshore structures in the arctic and subarctic regions are vulnerable to a variety of natural hazards (Ramadhani et al., 2022). Global ice and local ice loads must be considered to ensure safe operations and installations in the artic and sub-artic regions (Palmer et al., 2012). Icebergs originally from Greenland drift south towards Newfoundland and Labrador and Grand Bank's development field. This movement is influenced by ocean current velocity, wind velocity, and iceberg size (Wagner et al., 2017). One of the risk factors associated with iceberg drift is the probability of scouring offshore bed or installations (Croasdale et al., 2019). In addition, risk of iceberg interactions with offshore facilities must be appropriately accounted for to ensure safety of people and the environment. Hence, estimating ice loads for design against such forces and environmental loads is essential. Meltwater from icebergs provides a crucial freshwater flow from the ice sheet to the sea (Davison et al., 2020), accounts for 45% of Antarctic freshwater losses, and dominates the freshwater production in Greenland (Hester et al., 2021). Melting ice shelves into the ocean reduces the salinity of the water at the immediate vicinity, which may pose threat to marine life.

1.2 Background

Ice scallops or cuspate surfaces are 5–20 cm semi-intermittent waveforms at ice-water interfaces within a soluble material (Bushuk et al., 2019a). A scallop is a term used to describe a type of surface melting of glacier ice. Different factors may influence scallop formation, including water depth, ocean current, fluid viscosity, and temperature gradient. Previous research has discovered that scallop structures are due to a self-strengthening connection between an advancing ice-surface geometry, a turbulent stream field, and the subsequent differential melting rates along with the fluid-ice interface. Ice load estimation and its scale effect are critical considerations for ice loss, ship, and structure design. The formation of scallops may affect such interactions, and it is imperative to understand the conditions that influence the formation and the shape of these scallops at the ice-water interfaces.

Figure 2.1(a) shows an image illustrating the interaction of the scalloped ice surface with a structure. The abbreviations *hpz* and *lpz* represent high-pressure zones and low-pressure zones, respectively. AL_o is the nominal local ice area, while AL_S represents the local area of the scalloped ice surface. The crest of the scalloped surface is in direct contact with the structure upon impact, resulting in high pressure around the crest. Most of the force is transmitted in condensed regions known as high-pressure zones (Jordaan, 2000).

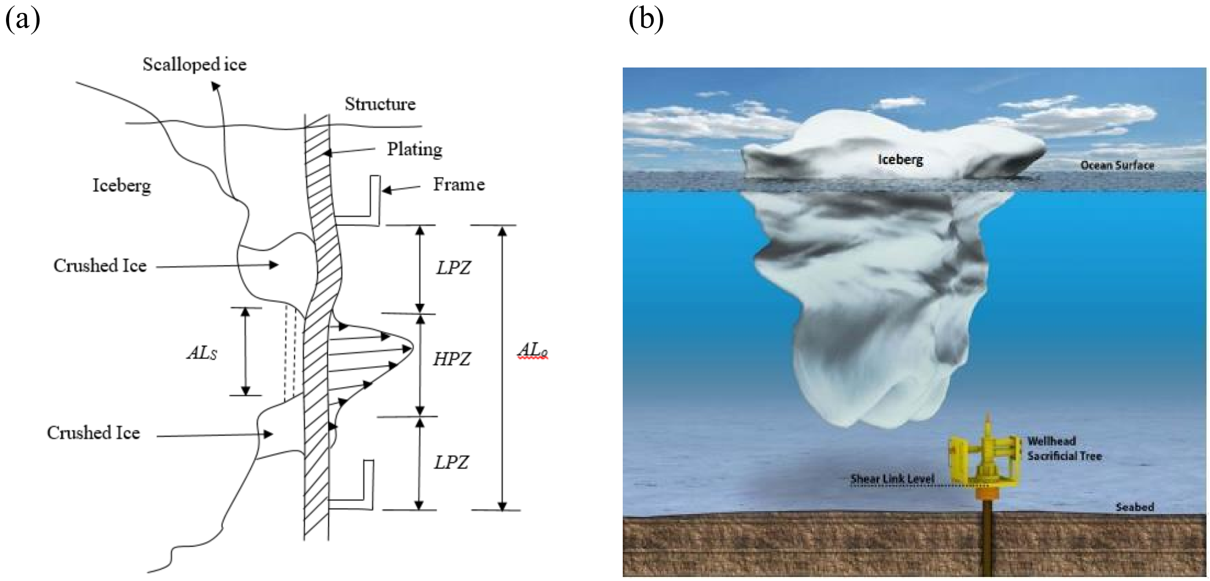

Fig. 1.1 (a) Schematic of iceberg-structure interaction showing high pressure zone (*hpz*), surrounding low pressure zones (*lpz*) that occur when an ice scallop with contact area ALS acts on a local design area AL_o (dashed lines represents progression of scallop contact area development during crushing (b) gouging of ice, an iceberg in contact with offshore subsea equipment (Budwit-Hunter, 2015).

Ice crushing failure dominates the design of structures with vertical surfaces subjected to ice loads (ISO, 2019). This study investigates how these scalloped surfaces are formed to help explain the condition under which the formation of these features is expected to occur.

1.3 Objectives of the Research

The primary objective of this study is to investigate the phenomenon leading to the formation of scallops in the context of local ice pressure. Secondly, the report will present analytical modeling and simulation of scallop ice formation. This will highlight the flow structure around simulated ice. The study will also investigate the Reynold number effect on scallop wavelength, temperature profile, and differential melting.

1.4 Research Questions

The key research questions to be considered in this study include the effect of temperature on the formation of scallops, and how the Reynolds number influences scallop formation.

1.5 Scope and Outline of Research

This study investigates the formation of scallops through analytical modeling, simulation, and experimental methods. This includes a review of related literature to determine the various approaches used in the past and how it affect the outcomes. A small-scale laboratory experiment was conducted in which a rectangular ice block sample was mounted in a flume tank in the fluid laboratory of Memorial University of Newfoundland and Labrador. A model is formulated and simulated using commercial software for different flow conditions. The study aimed to investigate scallop formation for different Reynolds numbers, temperature profile within the melting ice, to study vortices or flow structures within the domain of the scallops, and the effect of Reynolds number on the wavelength of the intermittent features.

The thesis is divided into seven chapters: introduction, literature review, numerical methodology, experimental method, results and discussion, conclusion, and recommendations, as summarized below:

Chapter 1: This chapter introduces the background and need for the research work. It outlines the objectives of the work. The scope of the thesis is described to address the knowledge gaps from related literature.

Chapter 2: This chapter considers a comprehensive review of related literature on relevant research areas. It includes a review of various methodologies used to experiment with melting ice as well as turbulence models.

Chapter 3: A detailed experimental approach and methodology are presented in chapter 3. The instrumentation used to obtain the required data and results are also described thoroughly. This chapter explains the ice sample-making process and experimental procedure. The experimental uncertainties are also outlined.

Chapter 4: A detailed numerical methodology/approach is described here. It includes the enthalpy-porosity method and the multiphase fluid flow models.

Chapter 5: This chapter presents and compares experimental and numerical results. Plots of melt front of the simulated ice, experimented ice are illustrated and described in this section.

Chapter 6: In Chapter 6, a detailed discussion and analysis of results are included. Comparisons between plots of different Reynolds numbers are presented and discussed. The melt rates of the three Reynolds numbers are compared and discussed in detail. The experimental results and explained and compared with the simulated results to enhance the understanding of the differential melting of the ice.

Chapter 7: Conclusions are summarized, and recommendations are made for future work.

Chapter 2: Literature Review

2.1 Overview

Knowledge of ice and its behavior must be considered when designing for local and global ice pressure in ice environments. The general shape and size of icebergs are described using standard descriptions (MANICE., 2005a) and the shape may be classified as domed, tabular, pinnacled, dry-dock, blocky or wedged, while size may be categorized as: growler, bergy bit, small, medium, large, and very large bergs. While new technologies for capturing detailed global iceberg geometry offer much higher resolution information (McGuire et al., 2016). Icebergs severely threaten offshore minerals production, navigation, and transportation (Chung, 2001). Icebergs can be classified as domed, tabular, pinnacled, dry-docked, or blocky and wedged. Icebergs vary in size and are categorized as small, medium, large, and very large. A flat-topped iceberg with steep vertical sides is referred to as a blocky iceberg, domed icebergs are identified by their above-water roundness, and they generally have smooth surfaces. Dry-docked icebergs typically have two pinnacles and a u-shape formed near the water level (Manice, 2005). This section presents a comprehensive review of experimental and numerical approaches to investigating the formation of ice scallops.

2.2 Review of Fundamental Fluid Mechanics

Considering a fluid stream with initial velocity u_i, approaching a piece of ice with some components passing by the opposite sides while a portion of it flows beneath the surface. The instantaneous velocity, U_i is plotted against time, as shown in Figure 2.1. Partial differential equations was derived to characterize the chaotic behavior of the liquid as it encounters the piece of ice.

Figure 2.1 shows the average and fluctuating velocity components of fluid.

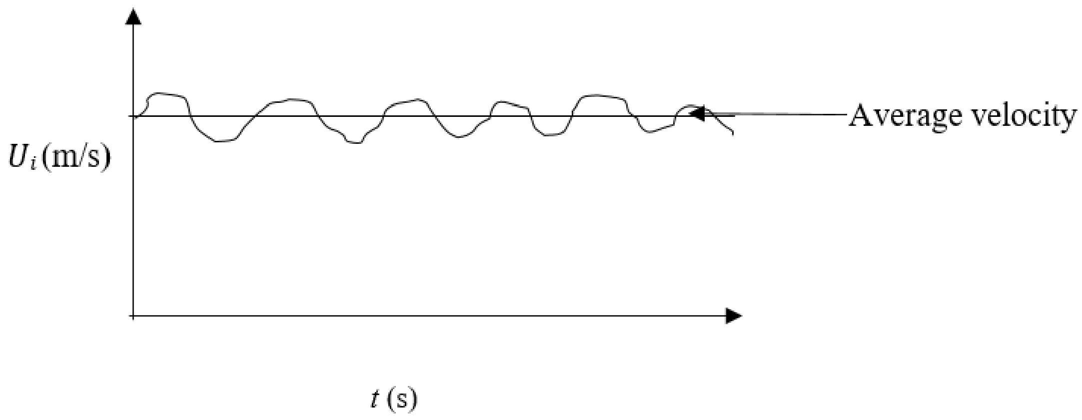

Figure 2.1: Average and fluctuating velocity of an approaching fluid

The fluid under consideration is assumed to be incompressible. The Naiver stokes equation governs the flow of viscous incompressible flows towards the rectangular block of ice as in equations 2.1

$$\frac{\partial u_i}{\partial t} + \frac{\partial (u_i u_j)}{\partial x_j} = \frac{-\partial p}{\partial x_i} \mathrm{v} + \frac{\delta^2 u_i}{\delta x_j \delta x_j} \tag{2.1}$$

$$\frac{\delta u_i}{\delta x_i} = 0 \tag{2.2}$$

where ν represents the kinematic viscosity of the fluid, u_{ij} is the fluid velocity, and p is the pressure of the fluid. Using the concept of Reynolds decomposition, the dependent variables, u and p, are decomposed into the mean and fluctuating terms, as shown in equation (2.3).

$$U_i = \bar{u} + \acute{u} \qquad\qquad P = \bar{p} + \acute{p} \tag{2.3}$$

U_i is the instantaneous velocity of the fluid, $\bar{u}$ is the time average of the velocity, and u' represents the fluctuating component of the velocity. Deploying the Reynolds averaged Navier-Stokes equation, a partial differential equation system that governs the pressure fields and the mean velocity of incompressible turbulent flow is given by equation 2.4.

$$\frac{\partial(\rho u_i)}{\partial t} + \nabla\cdot(\rho u_i u_j) = -\frac{\partial p}{\partial x_i} + \nabla.[\mu(\nabla u_i + (\nabla u_i)^T)] + \rho g - \nabla\left(\frac{2}{3}\mu(\nabla.u_i)\right) - \nabla\cdot(\rho \acute{u}_i\, \acute{u}_j) \tag{2.4}$$

The first term in equation 2.4 represents the transient term, the second term is the convection /advection term, and the last term on the right side of the equation is the stress tensor. The stress tensor term is unknown, hence the need to find this term to close the equation. The stress tensor is a product of two fluctuating fluid velocity components averaged over time. The first term on the right side of the equation is the pressure acting on a fluid particle, and the middle term is the external body forces.

$$\begin{bmatrix} u_1^2 & u_1 u_2 & u_1 u_3 \\ u_2 u_1 & u_2^2 & u_2 u_3 \\ u_3 u_1 & u_3 u_2 & u_3^2 \end{bmatrix} \tag{2.5}$$

Equation 2.5 is the Reynolds stress tensor; the parameters u_1^2, u_2^2, u_3^2 at the diagonal represent the normal stress, while the other parameters are the shear stresses present in the fluid. The stress tensor matrix is symmetric about the diagonal and $u_i u_j = u_j u_i$; hence, we have six to determine and the mean velocity fields. Closing the RANS equation requires expressing the stress tensor in quantities or parameters that can easily be determined. This study uses the Boussinesq hypothesis of eddy viscosity to complete the RANS equation given in equation 2.6

$$\frac{\partial \bar{u}}{\partial t} + \nabla.(\bar{u}\bar{u}) = -\frac{1}{\rho}\left(\nabla\bar{p} + \frac{2}{3}\rho\nabla k\right) + \nabla.\left[\frac{1}{\rho}\left(\mu + \mu_t\right)\nabla\bar{u}\right] \tag{2.6}$$

The Boussinesq hypothesis relates the Reynolds stress tensor to the mean velocity gradient of the fluid. The mean velocity gradient is the first term on the right side of the equation (2.6). The μ_t is the kinetic

The fluid under consideration is freshwater. It is assumed the fluid under consideration is incompressible. The conservation laws, momentum, mass, and energy, describe the flow. The equations 2.7, 2.8, and 2.9 are Navier stokes equations in *x, y*, and *z* directions, respectively, illustrating the mean flow velocities and the continuity equation.

Momentum in the *x*-direction

$$\frac{\partial}{\partial t}(\rho u) + \frac{\partial}{\partial x}(\rho uu) + \frac{\partial}{\partial y}(\rho vu) + \frac{\partial}{\partial z}(\rho wu) = - \frac{\partial P}{\partial x} + \mu(\frac{\partial^2 u}{\partial x^2} + \frac{\partial^2 u}{\partial y^2} + \frac{\partial^2 u}{\partial z^2}) \tag{2.7}$$

Momentum in the *y*-direction

$$\frac{\partial}{\partial t}(\rho v) + \frac{\partial}{\partial x}(\rho uv) + \frac{\partial}{\partial y}(\rho vv) + \frac{\partial}{\partial z}(\rho wv) = - \frac{\partial P}{\partial y} + \mu(\frac{\partial^2 v}{\partial x^2} + \frac{\partial^2 v}{\partial y^2} + \frac{\partial^2 v}{\partial z^2}) \tag{2.8}$$

Momentum in the *z*-direction

$$\frac{\partial}{\partial t}(\rho w) + \frac{\partial}{\partial x}(\rho uw) + \frac{\partial}{\partial y}(\rho vw) + \frac{\partial}{\partial z}(\rho ww) = - \frac{\partial P}{\partial z} + \mu(\frac{\partial^2 w}{\partial x^2} + \frac{\partial^2 w}{\partial y^2} + \frac{\partial^2 w}{\partial z^2}) \tag{2.9}$$

Continuity equation

$$\frac{\partial p}{\partial t} + \frac{\partial}{\partial x}(\rho u) + \frac{\partial}{\partial y}(\rho v) + \frac{\partial}{\partial z}(\rho w) = 0 \tag{2.10}$$

Acceleration due to gravity is represented by g in the expression. u, v, and w are velocity components in the x, y, and z directions. μ is the viscosity, t is time, T is temperature, and p represents pressure. Since the Boussinesq approximation is used, the properties of the liquid were assumed to be constant. Energy conservation can be applied to both quiescent and moving liquids, as it is affected by complex energy transfer mechanisms. The conservation of energy equation is defined as,

$$\frac{\partial}{\partial t}(\rho c_p T) + \frac{\partial}{\partial x}(\rho u c_p T) + \frac{\partial}{\partial y}(\rho v c_p T) + \frac{\partial}{\partial z}(\rho w c_p T) = k(\frac{\partial^2 T}{\partial x^2} + \frac{\partial^2 T}{\partial y^2} + \frac{\partial^2 T}{\partial z^2}) + q''' \tag{2.11}$$

q''' in equation 2.11 represents the volumetric heat generation rate within the control volume. c_p is the specific heat capacity. The first term on the left side of the equation represents transient energy while the term to the right of the equally to sign is the diffusion term. The dissipation term is represented by the last term on the right side of the equation.

2.3 Previous Experimental Ice-Scallop Studies

Bushuck et al. (2019) conducted a laboratory investigation on scallops and the ice-water interface. The experiment was conducted by deploying Particle Image Velocimetry in the refrigerated flume to quantitatively estimate the formation of ice scallops. Their investigation revealed three stages of ice-water interface evolution: a transition from the flat ice surface, an equilibrium scallop geometry, and adjusting the scallop interface. The rate of melt depends on the orientation of the ice and the direction of flow. The melting rate is higher on surfaces perpendicular to the direction of flow. They conducted their experiments in the Cold Region Research and Engineering Laboratory recirculation flume which was contained in a refrigerator with temperatures conditioned at 0 °C to ensure the ice was melting because of the temperature differences at the ice-water interface. Water was circulated in the flume at some specified volumetric flux. The water stored in a sump was re-conditioned by using heating and cooling coils when not in use. The volume flux and the flume were used to control the velocity of the fluid, as the flume could tilt at differential angles, as shown in Figure 2.2. A provision for measurement was made possible by using glass at the top and the side of the experimental setup. An ice sheet was freshly grown in a refrigerator for each experiment. Several tests were conducted by varying water temperature, bed temperature, and bed angle.

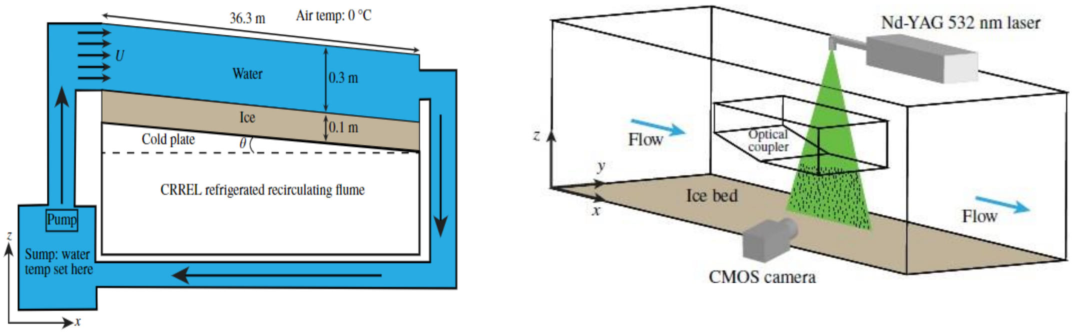

Figure 2.2: (a) setup for fluid circulation and mounting of ice (b) measurement region (Bushuck, 2019)

As shown in Figure 2.2, the experimental setup was designed to capture two successive images with illuminated particles lit up by a laser, allowing the velocity field to be computed by cross-correlation analysis of the consecutive images. A camera was placed perpendicular to the fluid flow direction to capture successive shots at a pre-determined laser pulse rate. The camera was intermittently moved along the flume to correct the pictures as the ice melted with time (Bushuk et al., 2019b). The collected images were analyzed using commercial PIV software (La Vision, DaVis 8.0). BCDVP was used to measure the vertical velocity component of the fluid in the well-developed scalloped region to allow for the computation of the heat flux (Koide et al., 2021).

Scallops are naturally occurring features found on surfaces of soluble materials. Richardson et al. (2005) observed multi-ripple features on an iceberg and referred to these features as cuspate. They investigated the influence of convective transfer as a scallop formation and facilitation medium. The study was based on the flow of air around an iceberg for which the melt rate was observed. The development of multi-ripple features on the surfaces of an iceberg was referred to as cuspate surfaces by Richardson et al. (2005). The influence of convective transfer as a medium for scallop formation and facilitation was studied. The study was based on the flow of air around an iceberg for which the melt rate was observed. Two forms of convective transfer were identified: cellular convection of air around the features and intercellular convection of air. It was observed that the air temperatures at the hottest hours of the day determine the size of the scallops shaped by the convection cells and that cellular convection dominates the melting process of the ice.

Presteau et al. (2009) used an experimental and numerical approach to study the formation of scalloped ice on the swept cylinder. Different swept angles were used for the simulation in an ice wind tunnel. Swept angle is the angle between the lateral axis and the quarter-chord line. The pressure in the tunnel was varied with the help of a low-pressure spray and high-pressure spray nozzle.

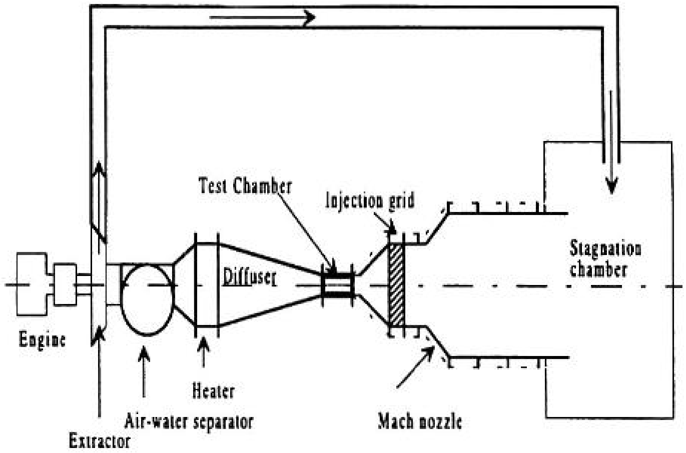

Figure 2.3: Wind Tunnel for studying the formation of scalloped ice on swept cylinder (Presteau et al., 2009).

The test presented in Figure 2.3 was conducted for a given parameter, T; all other parameters were kept constant. The temperature was one of the parameters identified, as a leading factor contributing to the formation of ice scallops. Swept angle variations were another parameter identified as contributing to variations in scallop ice formation. The authors confirmed the study and observation made by Virag et al. (2006). An experiment was conducted on the physical mechanisms of glaze ice scallop formations on swept wings. The team studied the influence of pressure, temperature, velocity, and cloud liquid water content (LWC). They concluded that the crossflow of fluid leads to the formation of the ice scallops observed by Virag et al. (2006). Curl (1974) investigated limestone-water and ice-air scallop patterns in caves. He observed that scallops tend to have a universal profile oriented along the direction of fluid flow, with their leeward sides having a steeper profile than their streamward sides. Curl (1974) proposed and concluded that scallops were observed when the Reynolds number was changed to 22500. The author also observed that scallops tend to propagate more within the mainstream of flow than the edges of the caves.

Recent studies point to the direction that water around ice shelves is shoaling into the ocean cavities, causing an increase in the melt rate of ice shelves (Jacobs et al., 2011). The heat and saline transfer across the turbulent boundary layer on the ice-ocean interface governs the rate at which sea ice and icebergs melt (Ramudu et al., 2016). Estimates of the melting rate at such interfaces range significantly across observational and modeling research to predict the evolution of sea ice and icebergs correctly (Cenedese et al., 2022); better constraints on their melting rate with the underlying flow are warranted. Basal melting produces a buoyant plume, generating turbulence and increasing the heat transfer rate (Little et al., 2009).

The flow field and diffusive properties in convective fluid flow led to mass and heat transfer distribution from surfaces. In the case of soluble characters, the interaction between the surface and the fluid flow leads to local dissolution, creating new boundary conditions for the adjacent fluid interaction (Blumberg et al., 1974). Ramudu et al. (2016) experimented on time evolution and ice melting in a turbulent shear flow, inducing melting because warm water flows to the ice-water interface. Particle image velocimetry was used to obtain the velocity of flow. The experiment was divided into three different phases. The first phase consists of freshwater sitting in a containing vessel with a rotating lid. It also has a basal cooling plate that hosts solid rectangular ice serving as the control volume. The heat transfer rate to the ice was lowest as the turbulent later was above the ice regime. An increase in rotation of the lid saw a reduction in the stratified layer as the turbulent layer became dominant. The heat transfer rate during the third phase was observed to be highest as a turbulent layer of the fluid stream became dominant over the stratified later. It is evident that the presence of turbulence in a flow field increases the rate of heat transfer. However, the experiment was conducted using fresh water. Since most development in the Grand Bank's development field is in saline water, it will be appropriate to consider the influence of saline water on the ice melting rate.

2.4 Review of Turbulence Models

Turbulence models are reviewed to understand and implement the appropriate model for solving the ice-water moving boundary problem. Most industrial and engineering flows are turbulent (Escudier, 2017). Applications such as fluid dynamics and heat transfer through pipes, turbines, heat exchangers, and boilers involve the application of turbulent flows. Turbulence consists of a continuous spectrum from small to large vortices and a superposition of discrete regions where the laminar flows (for example, back to the laminar flow). Each vortex represents a coherent cluster of liquid atoms or molecules that roam in unison (Riglin et al., 2021b).

Turbulence is the dynamic overlap of a large number of vortices with a random (irregular) continuous size spectrum at velocities, interspersed with small discrete pockets of laminar flow (Kolmogorov vortices). The same applies to viscous laminar flow sublayers and intermittent boundaries resulting from collapse (Riglin & Reid 2021).

In turbulence models, since the velocity fluctuates with time, the equations are decomposed into instantaneous and fluctuating velocities and averaged over time, thereby simplifying the mathematics of the eddies (Launder, 2015). Hence, the new governing flow equations include the sum of fluctuating and time-average quantities.

The Reynolds stresses are expressed in terms of known average quantities, such as the Boussinesq hypothesis, by establishing the relationship between Reynolds stresses and velocity gradients through eddy viscosity (van et al., 2010). In addition to the Boussinesq theory, the Reynolds stress model is used for turbulent closure.

From the momentum equation, the additional term indicates Reynolds stresses, which are fluctuating components, $-\frac{\partial}{\partial x}(\rho\overline{v'u_i'})$ This term represents the effect of turbulence on mean-time quantities. The new term -$\frac{\partial}{\partial x_i}\left(\rho c_p\overline{T'u_i'}\right)$ The energy equation represents the heat flux, which is the fluctuating temperature and velocity (Riglin et al., 2021a). In tensor notation, the stress is indicated as $\overline{u_i^{'}u_j^{'}}$. The Eddy-viscosity model proposed by Boussinesq can be used to analyze the turbulence closure (Shi et al., 1999).

2.4.1 Zero Equation Model

The zero-equation or algebraic turbulence model does not require the additional transport closure equation, so the naming convention is zero. Prandtl hypothesized the mixed-length hypothesis. The mixture length model assumes a relationship similar to molecular transport with the movement of liquid masses (Chen et al., 1998). The zero-equation model is robust and easy to code. The shortcomings of this model include minimal applicability. They are excellent for thin boundary layers but flatten out of the intended limited space (Shi et al., 1999). They do not provide turbulent scale transport of velocity, length, or other variables (Gualtieri et al., 2017).

2.4.2 One-Equation Model

One equation model is based on a turbulent transport quantity, turbulent kinetic energy k, partial differential equations, and a closure expression. Ludwig Prandtl developed one equation model turbulence closure using k as a transport quantity (Taylor et al., 2005a). The kinetic transport equation is given in equations 2.12 and 2.13.

$$\frac{\partial k}{\partial t}+\overline{u}_{\mathrm{j}}\frac{\partial k}{\partial x_j}=R_{ij}\frac{\partial \overline{u_i}}{\partial x_j}-\varepsilon+\frac{\partial}{\partial x_j}\left(\left(\upsilon+\frac{\upsilon_t}{\sigma_k}\right)\frac{\partial k}{\partial x_j}\right) \tag{2.12}$$

$$R_{ij}=\upsilon_t\left(\frac{\partial \overline{u_i}}{\partial x_j}+\frac{\partial \overline{u_j}}{\partial x_i}\right)-\frac{2}{3}k\delta_{ij} \tag{2.13}$$

where ε represents the dissipation rate of the turbulent kinetic energy and k represents turbulent kinetic energy.

The turbulent viscosity and the eddy length scale proposed by Prandtl are outlined below for turbulence closure. The dissipation rate ε is obtained from equation 2.14.

$$\varepsilon=\frac{C_D k^{\frac{3}{2}}}{l} \tag{2.14}$$

$$\upsilon_t=lk^{\frac{1}{2}} \tag{2.15}$$

where $l = \kappa y$, κ (von Karman constant) = 0.41, and σ_k = 1, for shear flows, the value of C_D is normally taken as 0.3 (Ni et al., 2013).

2.4.3 The *k*-*ε* Model

This approach uses the variable component of the velocity in three coordinate directions to obtain successive turbulent kinetic energies (Ivanova et al., 2013). This model makes use of two transport equations (Schmitt, 2007). The *k* equation is given by equation 2.16.

$$\frac{\partial k}{\partial t}+u_j\frac{\partial k}{\partial x_j}=\frac{\mu_t}{\rho}S^2-\varepsilon+\frac{\partial}{\partial x_j}\left(\frac{1}{\rho}\left(\mu+\frac{\mu_t}{\sigma_k}\right)\frac{\partial k}{\partial x_j}\right.\tag{2.16}$$

while the epsilon equation is obtained from the NS equation;

$$\frac{\partial \varepsilon}{\partial t}+u_j\frac{\partial \boldsymbol{\varepsilon}}{\partial x_j}=\frac{\varepsilon}{k}\left(C_1\frac{\mu_t}{\rho}S^2-C_{2\boldsymbol{\varepsilon}}\varepsilon\right)+\frac{\partial}{\partial x_j}\left(\frac{1}{\rho}\left(\mu+\frac{\mu_t}{\sigma_\epsilon}\right)\frac{\partial \varepsilon}{\partial x_j}\right.\tag{2.17}$$

Where $\boldsymbol{\varepsilon}$ represents the turbulence dissipation rate, and it's the rate at which energy is lost out of the system under consideration. *k* is the turbulence kinetic energy, and μ_t is the turbulent viscosity of the transport medium.

2.4.4 *k*-*ω* Turbulence Model

This model is an empirical model based on the transport equation for turbulent kinetic energy and the associated dissipation rate, expressed as the ratio of the epsilon equation to the turbulent kinetic model expression. Although the *k*-*ε* model has been successfully computationally modeled, it has drawbacks in some situations. In particular, the *k*-*ε* model performs better away from the main flow wall. However, there is a problem in the boundary layer zone, especially if the Reynolds number is low (Ivanova et al. 2016). The SST-*k*-***ω*** model ensures a smooth transition from the near wall to the inner domain of the fluid flow.

2.4.5 Large-Eddy Simulation (LES)

In contrast to the Reynolds average Navier-Stokes method, the LES uses a filtered Navier- Stokes equation (Tang et al., 2019). Equation filtering is the process of filtering vortices on a scale smaller than the filter width, thus spaces between the grids, leaving behind equations that model only the dynamics of large vortices. The LES model uses the filtered equation to solve large eddies directly in a time-dependent simulation and is more computationally expensive; thereby, turbulence with a small standard reduces the inaccuracy caused by modeling the flow. Large vortices obtain kinetic energy from the primary fluid energy. It contains most of the turbulent kinetic energy. It cascades the kinetic energy by stretching or breaking it into small vortices of the most diffusion processes involving mass, turbulence, and energies. Large-eddy simulations are highly desirable in near-wall flow resolution (Riglin et al., 2021b).

2.4.6 Direct Numerical Simulation (DNS)

DNS is a turbulence modeling technique that solves the unsteady Navier-Stokes equation to resolve all turbulence scales. Unlike LES, the sub-lattice model is not used (Rolfo, 2010). As a result, DNS is computationally expensive. DNS is unique among turbulence models in that it does not use averaging. DNS uniquely solves Navier Stokes to compute the variation of all instantaneous primitive variables.

2.5 Review of Sample Numerical Work

Scallops are formed naturally when a fluid flows over the surfaces of soluble materials; the fluid can either erode the surfaces or transport some material. There can also be a thermodynamical effect on the melting of the surfaces (Richardson et al., 2005). Thorness et al. (1979) provided insight into turbulence analysis of ice-water interface instabilities. They considered the transfer of mass and heat between a fluid and a small amplitude solid wavy surface. They identified $2000\upsilon / u^* < \lambda < 18000v / u^*$ for ranges of wavelengths for a melting surface and $2000\upsilon / u^* < \lambda < 18000v / u^*$ for ranges of wavelength for which most unstable wavelengths occur, where λ represents the scallop wavelength. There have been theories suggesting and attributing the formation of scallops to initial perturbations at ice surfaces. Bushuk et al. (2019) debunked these schools of thought. Claudin et al. (2017) built upon Hanratty's (1981) work by considering the effect of surface roughness.

Bushuk et al. (2019) used the fluid-structure equation developed by Stephan (Little et al., 2009). It involves the interaction between ice and water in which the turbulent flow field and resulting heat transfer either melts or freezes the ice-water boundary layer. Equation 2.19 was based on analyzing their laboratory results. Navier–Stokes equations for non-hydrostatic 2-D (x; z), homogeneous incompressible flow governs the water aspect of the domain. ρ represents the pressure of the fluid, u is the water velocity field, $\check{k}$ is the thermal diffusivity of the liquid.

The water is modeled as a constant density quantity. Freshwater was used while neglecting the buoyant term in equation 2.1. The temperature evolution in the water field is governed by equation 2.18.

$$\frac{\partial T_w}{\partial t} + u.\nabla T_w = \nabla.(K_w \nabla.T_w) \tag{2.18}$$

The melting and freezing of ice are governed by heat conservation across the ice-water interface.

$$Q_w - Q_i = \rho_w c_p k_w \nabla T_i \acute{\eta}|b = \rho_i \dot{M} L \dot{\nabla}\, T_w . \acute{\eta}|b - \rho_i c_p k_i \tag{2.19}$$

where Q_w and Q_i are heat flux across the water stream and ice, respectively, $\dot{M}$ is the melt or freezing rate, depending on its sign. The positive sign signifies the freezing of water, increasing ice thickness, while a negative flag means ice melting. Claudin et al. (2017) investigated the formation of scallops when a fluid flows around a soluble material theoretically. The model was divided into several parts. Their first model used the turbulent model with flow over a solid surface. The second model describes the melting process using advection-diffusion scalar transport with a standard mixing length approach. The equations are linearized with a small perturbation with a sinusoidal input, providing the disturbance growth rate and propagation velocity. A van Driest-like mixing length was adopted to account for rough and smooth regimes (Pope, 2000) as in equation 2.20.

$$l = \kappa(z + r_{\mathrm{d}} - Z)(1 - \exp(\frac{\tau_{xz}}{\rho})^{\frac{1}{2}}(\frac{z + sd - Z}{vR_t})) \tag{2.20}$$

where R_t is the van Driest transitional Reynolds number approximately equal to 25, r_d corresponds to the standard Prandtl hydrodynamical roughness.

Gilpin et al., (1980) investigated the wave formation and heat transfer at an ice-water interface in a turbulent flow. They investigated the source and conditions for instability for a well-developed turbulent boundary layer flow. A schematic of the diagram employed in their analysis is shown in Figure 2.4.

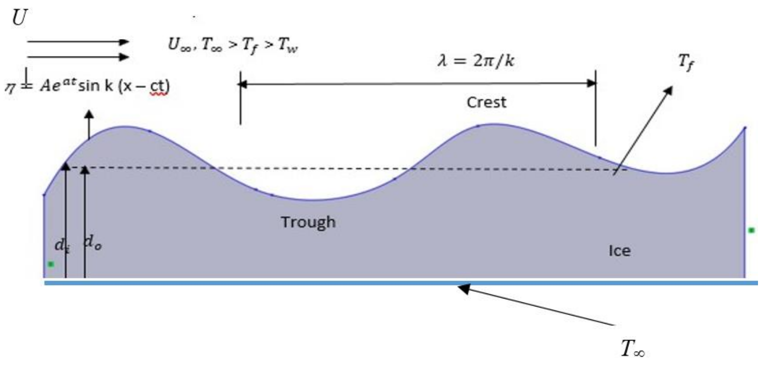

Figure 2.4: Schematic diagram of ice-water turbulent boundary-layer flow

U_∞ represents the initial turbulence flow velocity, the temperature of the ice-water interface is represented by T_f in Figure 2.4. The mean diameter of the ice sheet is represented by d_o. The mean thickness and the perturbed surface give the local ice thickness. The heat transfer coefficient, h, at the surface is given by $h = h_o + h_1$ where h_o is the mean heat transfer coefficient and h_1 is the displacement value. A heat balance equation on an ice-water surface is given in equation 2.21:

$$\rho L \frac{\partial d_i}{\partial t} = K_i \frac{\partial T}{\partial y}\Big|_{y=d_i} - h(T_\infty - T_f) \tag{2.21}$$

where ρ represents the density of the fluid, K is the coefficient of thermal conductivity, T_∞ represents the mean temperature of the surface of the ice and T_f is the temperature of the ice-water interface. Linearizing and integrating into the model the evolving boundary conditions, the model reduces to;

$$\rho L h_o (T_\infty - T_f) \frac{\partial d_o}{\partial t} = k_i \theta h_o d_o - 1 \tag{2.22}$$

where $\theta = \frac{(T_f - T_w)}{(T_\infty - T_f)}$.

The growth rate of the ice features was modeled as the ratio of the heat flux away from the interface into the ice to the heat flux from the water to the interface given by equation 2.23.

$$\alpha = \frac{h_o (T_\infty - T_f) u^*}{\rho L v} k^+ + \left[-\frac{f \cos\phi}{k^+} - \frac{G}{\tanh k^+ + u^* \frac{d_o}{v}} \right] \tag{2.23}$$

where $k^+ = \frac{kv}{u^*}$, $G = 0$ and it represents the rate of amplification, u is found by relating Stanton number to the mean ice thickness and k^+ is a dimensionless quantity and K represents thermal conductivity.

u can be derived as in equation (2.24)

$$St = \frac{h_o}{\rho C U_\infty} = \frac{1}{P_r} \frac{k_i}{k_w} \frac{\theta}{G} \frac{v}{U_\infty d_0} \tag{2.24}$$

where St represents the Stanton number, P_r is the Prandtl number and ρ indicates the density of the fluid. In turbulent flows, the eddies ranges in length and time scale. The largest eddies are comparable in size to the mean flow characteristic length (shelf layer thickness, for example).

For a direct numerical simulation of engineering flows to be performed, a high resolution and corresponding run-time are needed for solutions nearly to or close to the Kolmogorov random flux length scale (Hanratty, 1970).The LES technique resolves eddies directly while modeling the small eddies. LES is thus between DNS and RANS in terms of the fraction of the scales that will be fixed (Taylor et al., 2005b). The following paragraph reviews some of the simulations carried out by the LES technique and their associated outcomes.

The turbulent flow was investigated in an open channel using the LES technique by T.G Thomas and J.J Williams from Engineering Queen Mary, Westfield college, and the University of London (Hanratty, 1970). The numerical simulation aimed to study turbulent flow through an open channel for which the surfaces can deform. Simulation of secondary motions caused by turbulent flow in an available channel at $B/H = 2$. The study was carried out using an LES code to allowed the free surface to deform, where B represents the width of the channel and H represents the height of the channel. A large Reynolds number was used with a resolution that produced results close to those obtained from physical measurements.

The results from the velocity profile plot compared the experimental data of (Stoesser et al., 2005) and (Tominaga et al., 1991) and computed LES and RSM. It also indicates corner contour structures because of secondary turbulence-driven current. The maximum mean velocity of 24.1 m/s for the computed LES compared with 24.6 m/s observed by (Stoesser et al., 2005).

The root mean square turbulent intensities for both measured and LES computed also showed a similar trend, with the intensities decreasing when approaching the free surfaces. From the results obtained, the conclusion can be drawn that LES closely matches the measured parameters and hence is a good technique for modeling and quantifying the turbulence behavior of flow-through channels.

The study investigated the turbulent flow structure over three-dimensional dunes through an open channel. The governing equations are discretized using the finite volume approach and grid staggering. A high-resolution scheme had to be developed to achieve high-order accuracy and monotonicity in the advection term (Darwish, 1993).The central difference technique determined the gradients of pressure and diffusion terms (Xie et al., 2013). Detailed measurements were made for turbulent flow over two of fourteen 3D dunes in a flume experiment. The computational model was designed to replicate the experiments undertaken and reported by (Maddux et al., 2003).

A 3D computational domain was used to simulate turbulent flow over 3D dunes with homogenous mesh and nodal height of the crest located at +0.225 m. The maximum water depth was maintained at 0.193m, while the ratio of the water depth to the maximum dune height, *h/H,* was 3.2. LES studies of turbulent open-channel flow have successfully applied no-slip boundary conditions to dune surfaces and assumed free characters to be rigid lids (i.e., free-slip boundary conditions), a technique already widely employed in previous LES studies (Xie, 2013). Three different kinds of grid sizes were used for the numerical simulation. The first one is a 256 mm × 128 mm × 80 mm grid, the second grid size measuring 352 mm ×176 mm × 112 mm, and the 448 mm × 224 mm ×160 mm grid. The velocity profile of these three mesh sizes was compared with that of the experimental. The results showed a better velocity profile regarding the Large-eddy simulation approach.

The velocity profiles for both simulated and experimental measurements were compared. The result shows a close resemblance of velocity profiles between the simulated and experimental for two different scenarios for the Reynolds numbers. Large-eddy simulation hence, can be used to simulate and closely mimic the experimental flow measurements.

This study presents simulation results of large eddy currents (LES) of flow in an open channel where a spherical layer roughens the channel bed. The roughness height, which corresponds to the diameter of the sphere, is 0.23 the depth of the channel l. The Reynolds number is based on mean friction velocity u^* and channel depth h, approximately 2820 mm. The flow sample was chosen to correspond to the laboratory experiments of (Detert et al., 2013). The mean velocities in the LES were compared with measured data. The calculated turbulence intensity distribution was evaluated by comparing them with experimental relationships for coarse-walled flows, as Stoesser et al. (2005) proposed. Spheres measuring 22 mm in diameter were placed at the channel's bottom. 1D acoustic Doppler current profiler (ADCP) was used to measure the streamwise velocities. Maddux et al. (2003) experiment measured the main flow characteristics. However, the model overestimated the Reynolds shear stress, mainly due to the periodic boundary conditions used in the simulation differed from the actual yield conditions in the experiments. A log-law plot for LES and experimental data shows were presented. The log-law plots show close average streamwise velocities between the investigation conducted by Stoesser et al. (2005) and that of the LES computed. These results agree with LES results from Xie (2013.) and Shi et al. (1999).

2.5.1 Review of Enthalpy-Porosity Technique

In this study, we deploy the Enthalpy-porosity technique to simulate the melting of ice as the model enables us to investigate the ice-water interface of the melting ice. This model uses convection-diffusion phase change with a fixed grid formulation to solve moving boundary problems. Ebrahimi et al. (2019), Koo et al. (2021) and Bouzennada et al. (2021), used fixed grid formulation to simulate flows.

The current model is based on enthalpy-porosity with a fixed grid to model the evolution of moving boundaries, focusing on introducing the mushy region (Voller et al., 1990). The mushy zone is the region in which the liquid fraction lies between 0 and 1. The porosity of 1 means the solidification of the fluid in the domain and vice versa.

The enthalpy of the material is expressed as;

$$H = h_s + \Delta H \tag{2.25}$$

h_s = sensible heat, and ΔH represents the latent heat of the material.

$$H = h_{reff} + \int_{T_{reff}}^{T} c_p dT \text{ (2.28)} \tag{2.26}$$

where h_{reff} is the reference enthalpy of the material, T_{reff} represents the reference temperature, and c_p is the specific heat at constant pressure.

The liquid fraction is given by;

$$\tilde{E} = \frac{T - T_{Solidus}}{T_{liquidus} - T_{Solidus}} \tag{2.27}$$

if $T_{\text{Solidus}} < T < T_{\text{liquidus}}$

$$\tilde{E} = 0 \text{ if } T < T_{solidus} \tag{2.28}$$

$$\tilde{E} = 1 \text{ if } T > T_{solidus} \tag{2.29}$$

The latent heat, ΔH is expressed in terms of the latent heat of the material, L as;

$$\Delta H = \tilde{E}L \tag{2.30}$$

The latent heat can vary between that of a solid (0) and a liquid (L). The energy equation for solidification/melting is expressed as;

$$\frac{\partial (\rho H)}{\partial t} + \nabla.(\rho u H) = \nabla.(k\nabla T) + S \tag{2.31}$$

where ρ represent the density and u is the fluid velocity. S is the source term, and H represents the enthalpy. The density is expressed as;

$$\rho = \rho_m(1 - W(T - T_{ref})) \tag{2.32}$$

where T is the temperature at the computational domain. W is a constant, $W = 9.2793 \times 10^{-6}$ $(°C)^{-q}$, T_{ref} is the reference temperature (Ghidersa, 2004). The momentum equation governs the fluid in the computational, but source terms are added to dump the fluid velocity whenever the domain solidifies.

The Darcy law governs the fluid in the mushy area, which is given by,

$$q = \frac{K}{\mu} \nabla p \tag{2.33}$$

where K is the permeability of the medium, q represents the instantaneous flow rate.

.

$$\nabla p = \frac{-C(1-\lambda)^2}{\lambda^2 \mu} \tag{2.34}$$

where $C = 1.6 \times 10^3$ depending on the porous medium's morphology, λ is the scallop wavelength and $q = 0.0001\text{m}^3/\text{s}$, to prevent division by 0 (Voller 1987). The source term is given by equation 2.35.

$$S = -\frac{(1-\tilde{E})^2}{\left(\tilde{E}^3+\nexists\right)} A_{mush}(u-up) \quad (2.35)$$

where $\tilde{E}$ is the liquid fraction, $\nexists$ is a small number to prevent division by 0, up is the pull velocity in the continuous casting process; in my studies, it was neglected. A_{mush} represents the mushy zone constant (Ansys Inc 2009). In the mushy zone, turbulence equations are modeled to include sinks. Sinks are added to turbulent equations to account for the presence of solids in a specific computational cell. The sink term added to the turbulent equations is given by;

$$S=\frac{(1-\tilde{E})^2}{\left(\tilde{E}^3+\nexists\right)} A_{mush}\emptyset \quad (2.36)$$

The turbulent quantities $(k, \emptyset)$ are represented by the letter $\emptyset$ in equation (2.37).

Considering the literature noted above, two main mechanisms of natural ice scallop formation may be identified: 1) buoyant convective flow effects; and 2) eddy effects on local melting rates. While the first mechanism is likely to play a more significant role under quiescent conditions, in the more turbulent environment found offshore it is expected that if ice scallops did form on an iceberg, they would likely be associated with eddy effects. Despite the work done, there is a need to investigate the ice-water interface of the melting ice. There is also a gap on the temperature distribution across the melting interface. Understanding the conditions that produce ice scallops and how these processes change as a function of mean fluid velocity is of particular interest. To this end, a series of experiments have been conducted to investigate ice scallop formation as a function of Reynolds number using rectangular freshwater ice block.

Despite the various numerical formulations and models, there is still work to be done on investigating the melting at the ice-water interface. In this study, enthalpy-porosity technique will be used to investigate the interfacial melting of ice.

Chapter 3: Experimental Setup and Procedure

3.0 Introduction

This chapter presents the methodology used for the experimental data collection. An experiment was carried out to investigate the mechanism for the formation of ice scallops. Scallops are ubiquitous in nature and are found some deformable bodies and mostly due to fluid-structure interaction. The section will involve vivid descriptions of the instrumentation used in the experiments. It also outlines and explains in detail the procedure involved in carrying out the experiment. Modifications were carried to the recirculation flume to help in mounting the ice specimen.

3.1 Experimental Design

This study required modifications of the recirculation flume and mold design to successfully mount the ice sample in the flume. Different concepts were developed to help mount the ice sample in the flume. Among the conceptual designs include a forced floor and hanging mold over the flume. A mold was fabricated in-house to accommodate the ice sample for testing.

3.2 Polycarbonate Mold

The mold was fabricated using a polycarbonate material via laser technology. The rectangular mold is 30 cm in length and 13 cm wide, and the height of the mold is 18 cm. Two pieces of pipes with similar dimensions to the inner diameter of the mold are placed inside the mold. They are arranged close to the ends of the mold. After solidifying the ice in the mold, a drill bit was used to drill out excess ice accumulation in the two pipes.

3.3 Description of Setup

The setup includes a centrifugal pump, a transparent rectangular channel, and a water reservoir. A recirculation flow channel was primarily used to conduct the experiment. The pump derives its energy from a power source. The reservoir stores water, which serves as the working fluid in the system. A Nikon camera was used to record the experimental process. A detailed description of the experimental setup is described in the next session.

3.4 Recirculating Water Channel System

The experimental setup consists of a reservoir where reserved fluid is stored. It also have variable frequency control, which controls the flow rate of water flowing through the channel. A flow pump is coupled to the system to force the working fluid to flow around the flume. The water flow channel is 390 mm in length and 294 mm in width. It has a glass cover on the side to help visualize the process in the channel during the experiment. The flume can handle up to 13 cm of water height even though the total flow height is 16 mm to prevent water spillage. The allowance is a precautionary measure to prevent water from spilling during the experiment. The far-right end has a gate used to control the average water depth. On the other hand, the far-left side has a constriction that introduces turbulence at the entrance to the channel, which is connected to a water hose. Figure 3.1 illustrates the setup for the experiment and the schematic diagram.

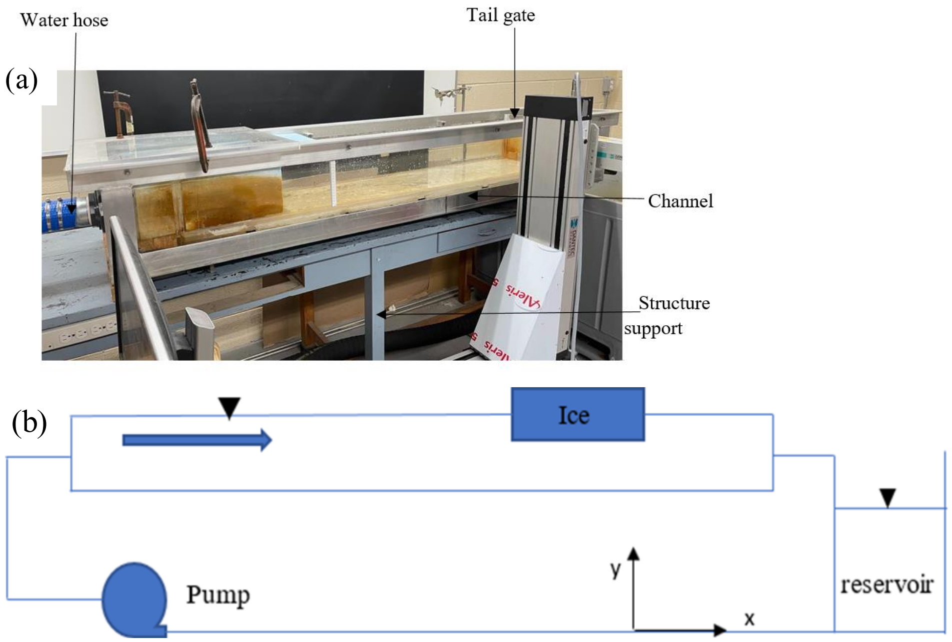

Figure 3.1: (a) Rectangular Recirculation flume equipped with perspex glass (b) Schematic of the experimental setup

The centrifugal pumps are self-priming units (up to 20 feet of stroke) designed for high-volume fluid transfer: irrigation, drainage, lawn irrigation, etc., or gases. The working pressures of the pump are up to 125 psi (862 kPa). The pump is equipped with a cast iron pump casing, a clog-resistant dual-flow semi-open stainless-steel impeller, and a cast iron adapter. The units are equipped with flap valves to ensure positive suction.

Figure 3.2: Centrifugal pump coupled to the recirculation flume.

A mechanical seal isolates the motor from the liquid in the pump casing. Units are mated with fully enclosed 3450 rpm fan-cooled motors. All units are manual models; controls are not included. The pump is connected to the power unit, and its speed can be changed by changing the frequency. The camera used throughout the experiment was Nikon D5600 with a single-lens digital camera and a Nikon F bayonet mount. It has a pixel size of 24.2 million with 23.5 mm × 15.6 mm with storage media and ISO sensitivity in 100 – 25,600. The camera supports autofocus with E type, AF-P and G AF-S lenses. It can shoot up to 5 frames per second with continuous top speed at full resolution.

3.5 Sample Preparation

Commercially produced ice cubes by the Brema ice maker were first stored in a refrigerator for several days and crushed into pieces using Clawson Model HQ-C Ice Crusher. Figure 3.3 shows a picture of the ice maker.

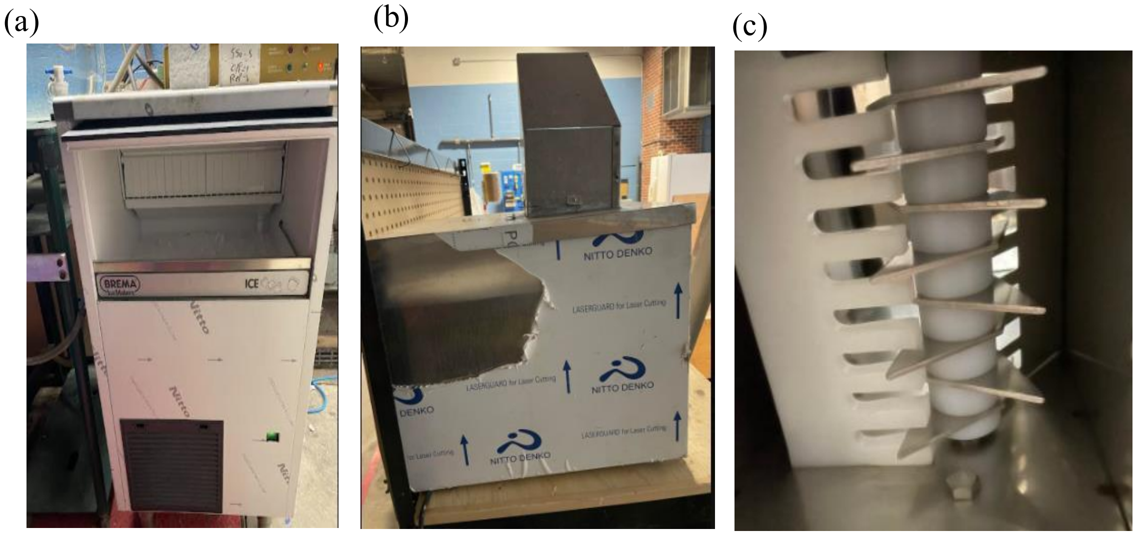

Figure 3.3: Equipment for sample making (a) brema ice maker, (b) clawson Model HQ-C ice crusher (c) arrangement of crusher teeth.

The crushed ice cubes were sieved using a 10 mm sieve. The sieved ice was placed in a bowl, and an amount of dye was added and stirred vigorously to ensure a homogeneous mixture to improve flow visualization. Some other samples were made without adding a dye. Chilled distilled water was added to the mix, and the slurry was transferred into the mold.

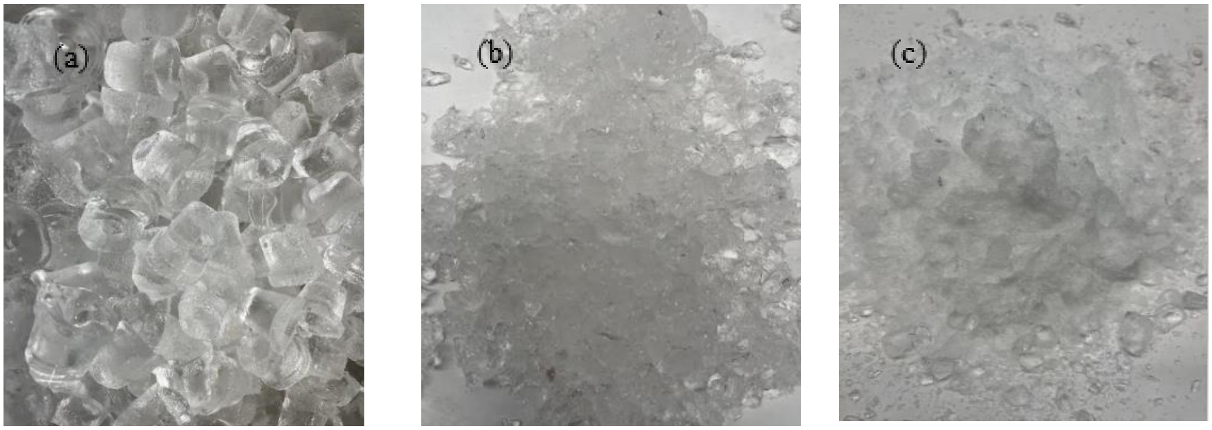

Figure 3.4: Ice same making process (a) seed ice (b) crushed ice (c) sieved ice

The slurry was carefully compacted and stirred to improve the expulsion of air bubbles. It was then transferred to the cold room, covered with Styrofoam, and left for 96 hours before the experiment. Styrofoam helps in the unilateral growth of the ice molecules and also helps in removing excess air from the ice-water mixture. Figure 3.4 (a), (b), and (c) shows pictures of ice seed samples, crushed ice after passing it through the Clawson Model HQ-C Ice Crusher, and sieved ice, respectively.

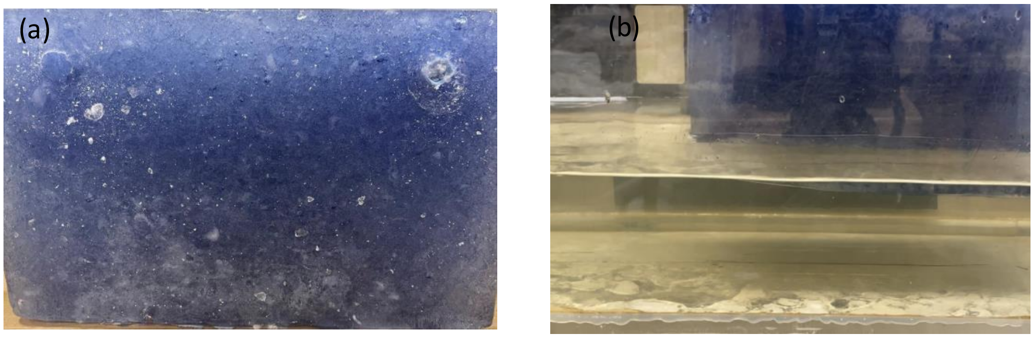

Figure 3.5: Ice sample mounted in the channel (a) ice sample, (b) sample mounted in a flume

Figure 3.5 shows an image of sample ice and a sample of the ice mounted in the flume. The surface of the ice was adjusted to flash with the middle of the channel where fluid velocity is maximum.

3.6 Experimental Procedure

Ice samples were removed from the cold room and transferred to the thermal lab for the experiment. Freshwater from the tap was channeled to the reservoir where the pump derives its supply. The water temperature was recorded for each experiment before and after the investigation. The water level in the tank was pre-determined by adjusting the gate at the exit of the flume and maintaining the water height at 13 cm. The Reynolds numbers investigated for the purpose of this study are Reynolds number ($2.3 \times 10^4, 3.00 \times 10^4$ and 3.30×10^4). The samples were transferred from the cold room prior to the start of the test. A drill bit was used to drill out excess ice accumulated in the pipes to create a way for rods to penetrate and helps in the mounting of the ice in the flume. An ice sample is arranged in the flume; the ice's surface aligns with the middle of the channel. The maximum velocity occurs in the middle of the medium. Water is then allowed into the track while videotaping the process with a Nikon 5600 digital camera. Table 3.1 shows a sample test matrix with different frequencies and their corresponding fluid velocities, hydraulic diameters, and Re numbers. The duration of each experiment is 10 minutes. The scallop's melt front was traced and measured with a contour gauge at the period's end.

Table 3.1: Experimental design

Frequency (Hz)	**Velocity (m/s)**	**$T_{initial\_water}$ (°C)**	**Hydraulic diameter (m)**	**Reynolds number**
15	0.142	15.24	0.181	23265
17	0.184	14.92	0.181	30147
20	0.200	13.68	0.181	32768

The procedure is repeated for each successive test conducted at 17 Hz and 20 Hz, corresponding to Re = 30147 and 32768, respectively.

3.7 Temperature distribution of the Ice

This study investigates how temperature variations along the ice sample affect the melt rate of the ice. Figure 3.6 illustrates the coordinate and sign conversion used to describe the direction of fluid flow through the channel. Four thermocouple wires were frozen into an ice sample 50 mm away from the front. The thermocouples are arranged vertically with 10 mm space between successive thermocouples as shown in Fig. 3.7. The water of initial velocity U_i is made to flow around the ice. Temperature readings are taken simultaneously after every minute until all the thermocouples fall into the water.

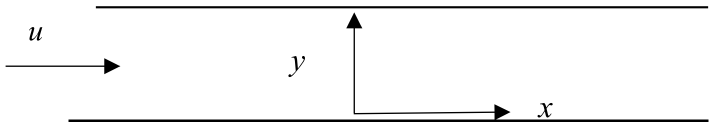

Figure 3.6: coordinate system and sign conversion for flow of fluid

where y (mm) represents spatial distance in millimeters, T (°C) is the temperature, $T_{ice\_initial}$ represents the initial temperature of the ice; $T_{w,al}$ is the final temperature of the water. $T_{\text{profile(front)}}$ is the temperature profile from the leading front of the ice and $T_{\text{profile(back)}}$ represents the temperature profile from the back of the ice.

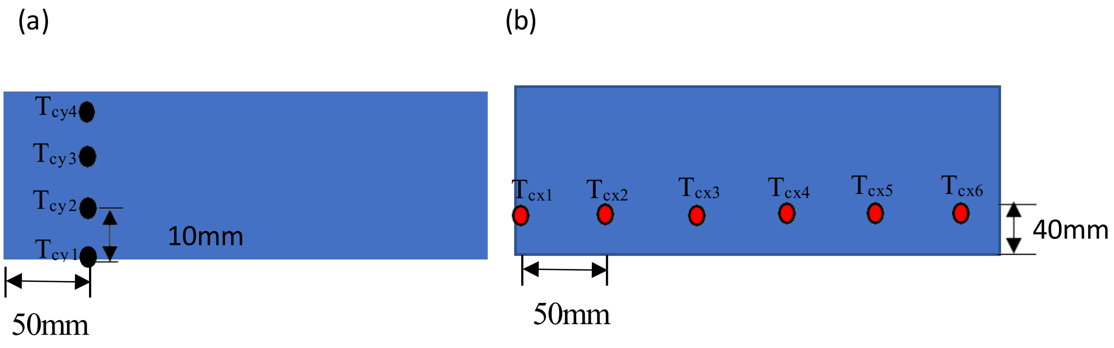

Figure 3.7: Thermocouples embedded in a piece of ice (a) vertical arrangement (b) horizontal arrangement.

Figure 3.7 represents images of thermocouples embedded in the ice samples. The thermocouples were arranged in horizontal and vertical directions. The horizontal and vertical thermocouples were placed 50 mm and 10 mm apart. The temperature data was taken from the sensors after every minute.

3.8 Sources of Error and Uncertainty

Data sets' errors are assessed to determine the confidence level of results. The errors are divided into two categories, namely, systematic/biased errors and random errors. Some sources of the frequent errors that impacted the results include errors from the thermometer and the thermocouple used to measure the temperature of the ice. Fluke, 52 II dual probe thermocouple, was used to measure the temperature of the ice prior to the experiment as well as the temperature of the water before and after the investigation. The initial and final water temperature has an accuracy of 0.05% ± 0.3 °C. A second source of error in the data set is the contour gauge, as the splines of the indicator could move slightly in drawing the scalloped profile. Table 3.2 shows an uncertainty table for the three Reynolds numbers data set. The data set is divided into three sections: the leading front, middle, tail, and chat to ensure unbiased analysis.

The results in Table 3.2 show a higher uncertainty for data sets at the leading front, followed by the middle data set. The least uncertainty was experienced in data sets at the tail end of the plot because the data is less spread.

Table 3.2: Uncertainty in scallop profile data set

Re 23265			
	Leading front (mm)	**Middle (mm)**	**tail end (mm)**
sample1	3.75±1.102	-6 ±1.452	-10.42±0.168
Sample2	4.07±1.23	-8 ±1.71	-12
sample3	5.86±1.19	-1.75±1.13	-5.58±0.17
sample4	1.29±0.69	-5.75±0.86	-6.5±0.57
sample5	2.07±0.74	-4.58±0.78	-4.83±0.66
Re 30147			
	Leading front (mm)	**Middle (mm)**	**tail end (mm)**
sample1	9.75±2.01	6±1.11	2±0.28
Sample2	6.5±1.92	3.83±1.52	-1.67±0.23
sample3	8.57±2.07	6.08±0.94	6.33±0.89
sample4	7.57±2.05	7.75±0.81	4.33±0.37
sample5	7.14±1.72	2.58±0.93	1.17±0.23
Re 32768			
	Leading front (mm)	**Middle (mm)**	**tail end (mm)**
sample1	9.75±2.01	6±1.11	2±0.28
Sample2	5.57±1.39	-4.25±1.96	-4.25±1.96
sample3	5.07±1.31	-5.75±2.05	-10.75±0.12
sample4	6±1.38	-4.08±1.99	-10.08±0.29
sample5	5.14±1.57	-3.50±2.75	-17.08±1.15

Chapter 4: Numerical Modelling

4.0 Introduction

This chapter describes the steps involved in numerical formulations and simulations of flows. The main aim of this study is to investigate the mechanism leading to the formation of ice scallops. From the literature review, the action of turbulence flow is largely associated with the development of undulating surfaces. The numerical model is divided into two sections: the first part involves fluid flow simulation in an open channel, and a model for simulating melting ice was formulated in the second section. Commercial software was deployed to simulate fluid flow through an open channel using the multiphase flow with the VOF technique.

4.1 Multiphase Flow in an Open Channel using the VOF Method

A multiphase flow model simulates two immiscible fluids, water and air, through a channel by solving a single set of momentum equations and tracking the volume fraction of each of the fluids throughout the domain. The simulation was initially carried out without air, but the results could not be validated using the law of the wall plot. The volume fraction parameter was set to an explicit scheme with two Eulerian phases. A pressure-based solver was used, and in the solution method, pressure-velocity coupling was used. The solution was controlled by setting the pressure to 0.5, momentum to 0.5, and volume fraction to 0.5. The volume fraction equation is used to track the interphase between the phases. The volume fraction equation is presented in equation 4.1.

$$\frac{1}{\rho_n}\left[\frac{\partial}{\partial t}\left(\alpha_n\rho_o\right)+\nabla.\left(\alpha_n\rho_o\overrightarrow{\vartheta_{q)}}\right)=S_{\alpha_n}+\sum_{o=1}^{n}\left(\dot{m}_{no}-\dot{m}_{on}\right)\right] \qquad 4.1$$

where $\dot{m}_{no}$ is then mass transfer from n to phase o and $\dot{m}_{on}$ is the mass transfer from phase n to phase o, where n and o represents solid and liquid phase respectively. S_{α_q} represents the source term in equation 4.1.

A single momentum equation is solved throughout the domain, and the resulting velocity field is shared among the phases. The momentum equation, shown below, is dependent on the volume fractions of all phases through the properties n and o.

$$\frac{\partial}{\partial t}\left(\rho\overrightarrow{\vartheta_q}\right) + \nabla.\left(\rho\vec{\vartheta}\,\vec{\vartheta}\right) = -\nabla_p + \nabla.\left[\mu(\nabla\vec{\vartheta} + \nabla\vec{\vartheta}^T\right] + \rho\vec{g} + \vec{F}$$

The limitations for the VOF approach includes, the use of pressure-based solver. The VOF model is not available with the density-based solver. Only one the phases could be defined as compressible ideal gas and the second-order implicit time-stepping formulation cannot be used with the VOF explicit scheme. In addition streamwise periodic flow, either specified mass flow rate or specified pressure drop, cannot be modeled when the VOF model is used.

4.2 Melting Modeling using Enthalpy-Porosity Technique

Table 4.1 shows the quantitative parameters used in the modeling and simulation. It shows the temperature range corresponding to each density, thermal conductivity, and specific heat capacity.

Table 4.1: Parameters for Melting simulation (Enthalpy-porosity modeling)

Temperature (°C)	Density (kg/m^3)	Thermal conductivity (W/mK)	Specific heat capacity (J/KgK)
-10	918.9	2.8	2000
-5	917.5	2.25	2027
0	916.2	2.22	2050
0.01	958.5	0.556	2217
2	999.6		
3			
5	837.54	0.5669	3200
7	999.89		
10	999.698	0.578	4191

For this study, the following constants were used in the implementation of the simulation. The viscosity of fluid was 0.001003m/s, the pure solvent melting heat = 333550 (J/kg) and the solidus temperature was set at -0.5 K.

The density corresponding to the temperature in Table 4.1 is computed using equation 4.1 to account for the maximum expansion of water at 4 °C (Niezgoda-Zelasko, 2016).

$$\rho = \rho_m (1 - 9.2793 \times 10^{-6})(T - 999.972)^{1.894816} \tag{4.1}$$

where ρ_m is 999.97kg/m^3 and ρ_m represents the maximum density of water at (4 °C). Figure 4.1 shows the numerical studied configuration for the simulation. A piece of ice with water flowing over the surface has a base temperature of Q_b. The heat of magnitude Q_w is applied at the top surface of the ice. The right and left sides of the ice are maintained at a constant temperature, -10

°C . The governing equations are discretized using the control volume approach.

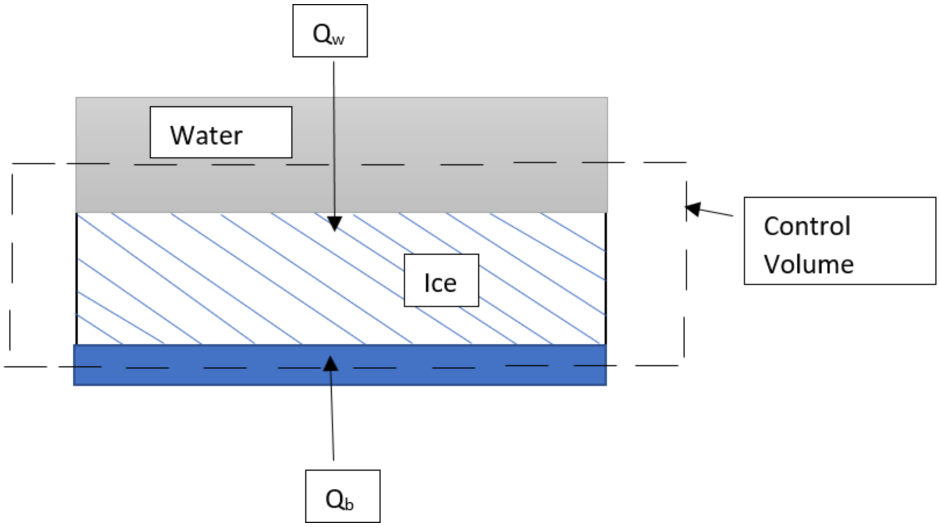

Figure 4.1: Computational domain

4.3 Open Channel Flow of Simulated Ice

Different mesh sizes were tested: a 1 mm mesh size, 3 mm mesh size, and 5 mm mesh size. Mesh sensitivity test was conducted to ensure accuracy of results and the result is presented in Figure 4.2. A 1 mm mesh size was selected as it produces the finest mesh and velocity profile. Figure 4.2 shows the boundary conditions generated for the simulation.

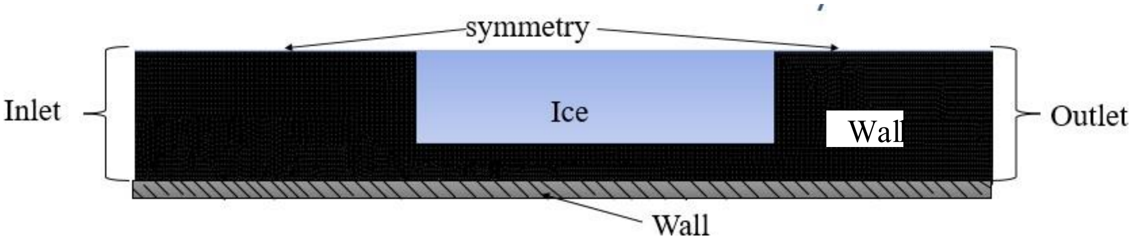

Figure 4.2 Boundary conditions

Table 4.2 shows the mesh resolution for the flow simulation. The element size and the number of nodes for a mesh size of 1 mm are 198929 and 200600, respectively. A mesh size of 0.8 mm was also considered but there was no significance difference between its velocity profile and that of 1 mm mesh size. The number of nodes and element size increases with decreasing mesh size.

Table 4.2: Mesh resolution

Mesh	**Nodes**	**Elements**
Fine mesh (1mm)	200600	198929
Medium mesh (3mm)	22943	22305
Coarse mesh (5mm)	8104	7729

Figure 4.3 shows a plot of the velocity profiles for a refined, medium, and coarse mesh. The velocity profile of a 1 mm mesh is observed to have a better resolution and the highest terminal velocity than that of the medium and coarse meshes.

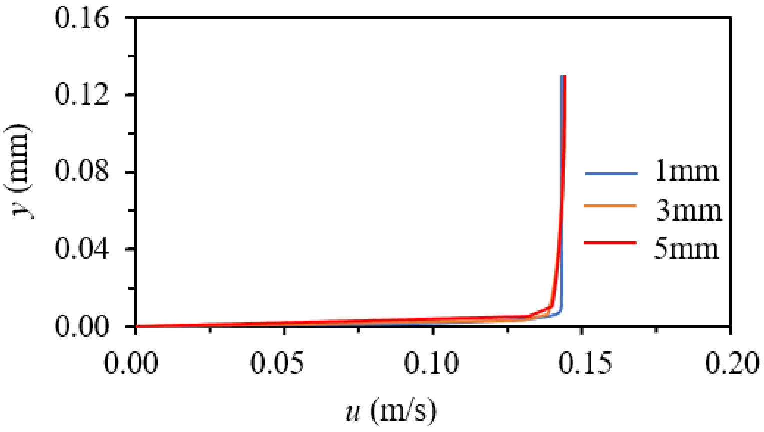

Figure 4.3: Mesh resolution for 1 mm, 3 mm and 5 mm mesh sizes.

The k-ε model was used as the model for the simulation. The geometry was meshed using the mesh control tool with a mesh size of 1 mm. Water was selected as the working fluid with cell zone conditions maintained as water. The SIMPLE scheme was deployed for pressure-velocity coupling. A bounded second-order upwind scheme was used for transient formulation and simulation. The solution was controlled by using the default under-relaxation factors in Ansys fluent. For convergence criteria, the continuity equation, horizontal velocity component, u, and vertical velocity component, v, were adjusted to 1×10^{-6} while the k and ε residual equations were adjusted to 1×10^{-5}. Standard initialization was used, and the horizontal velocity, *u,* was specified, corresponding to each Reynolds number. The maximum number of iterations per time step was specified as 100. Velocity profiles were extracted along a line at pre-determined positions from the solution.

Table 4.3 shows the boundary conditions implemented to simulate the flow of water around the ice. Water enters the channel at a specific velocity through the inlet of the channel, with no-slip conditions imposed on the walls of the channel and that of the ice. The outlet served as the pressure outlet of the channel while a symmetry boundary condition was assigned to the surface of the water in the channel.

Table 4.3: Boundary condition

Zone	**Boundary condition**	**Boundary values**
Inlet	Velocity inlet	0.142 m/s
outlet	Pressure outlet	-
Symmetry	Pressure inlet	-
Wall	No slip condition	-

Chapter 5: Experimental and Numerical Results

5.1 Overview

The experiment was divided into three main parts: the melting front of simulated ice, the effect of the Reynolds number on the ice's wavelengths, and the temperature profile of the melting ice. Five samples were tested for each Reynolds number. The melt front of each sample is presented as contour plots. The average contour plot of each test set was computed and compared relative to the Reynolds numbers. This chapter also outlines the Reynolds number's effect on the scalloped ice's wavelength. Each test set was conducted for 15 minutes, and the wavelength for each corresponding sample was measured with a meter rule. In addition, test samples were weighed on a scale before and after to determine how much ice had melted throughout the test. In addition, the results for the temperature distribution were presented.

5.2 Effect of Reynolds Number on Melt Profile

The initial temperature of ice was recorded in the cold room before the start of the test. The temperature of the initial ice varied from -5.8 °C to 7.8 °C with an average value of -7.04 °C.

A total of 15 samples were tested for each Reynolds number = 23265, 30147, and 32768 under specific test conditions. The test conditions for the first set of the experiment of Reynolds number 23265 are presented in Table 5.1. The initial temperature of the water ranges from 15.6 °C for Sample 1 through to 14.8 °C for Sample 5. The final water temperature of the water at the end of the experiment for sample 1 was recorded as 15.4 °C.

Table 5.1: Temperature of fluid: Reynolds number 23265

Sample	**$T_{initial\_water}$ (°C)**	**T_{final_water} (°C)**	**T_{ice} (°C)**
Sample 1	15.6	15.4	-7.8
Sample 2	15.4	15.1	-6.9
Sample 3	15.1	15.3	-7.7
Sample 4	15.3	14.8	-5.8
Sample 5	14.8	14.5	-7.0

Figure 5.1 represents the contour plot of the melt front for five samples tested under the measured temperature presented in Table 5.1. The area under the graph represents the volume of the basal melt, with the contour line indicating the surface geometry of the resulting ice front.

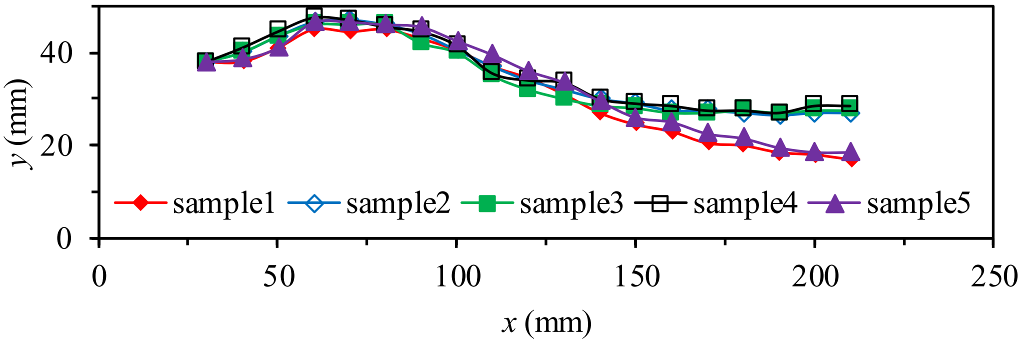

Figure 5.1: Melt front of ice for Re = 23265

The area to the left of the plot shows the frontal melt of the sample over the experimental time frame. However, the portion above the curve is occupied by ice left after the experiment. Figure 5.2 shows the average melt rate from the five samples, with the highest crest position at 46.3 mm relative to the trough position at 23.7 mm.

The crest position for the experiment set is identified to be 38 mm, while the trough varies from 46 mm for sample 1 to 46.5 mm for sample five. The highest trough height recorded was 47 mm, corresponding to the fourth sample. The differences between the trough and the crests are presented in Table 5.2, with an average difference representing the scallop height of 8.5 mm.

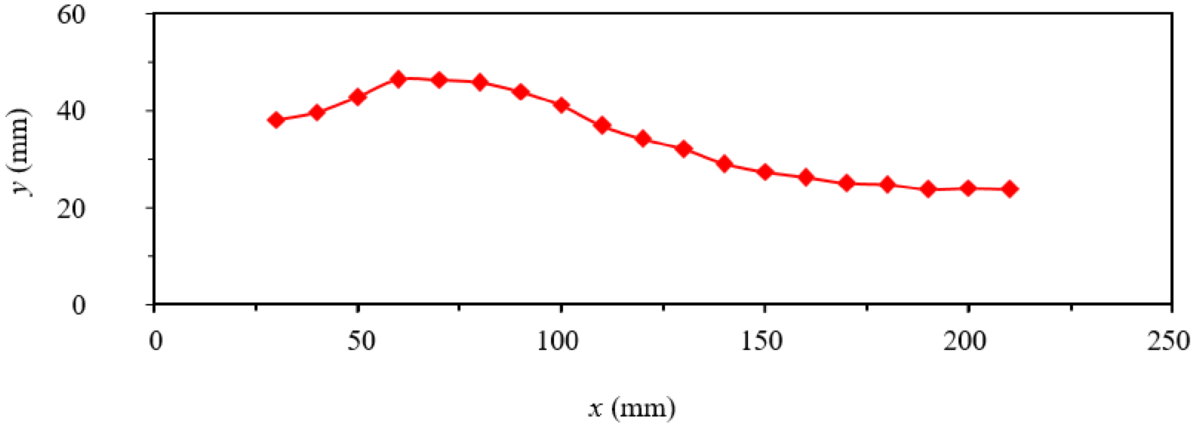

Figure 5.2: Average melt front, Reynolds number = 23265

Table 5.2 : Crest and trough positions, Re = 23265

Sample	**Crest position (mm)**	**Position of trough relative to the crest (mm)**	**Difference (mm)**
Sample 1	38	46.0	8.0
Sample 2	38	46.5	8.5
Sample 3	38	46.5	8.5
Sample 4	38	47.0	9.0
Sample 5	38	46.5	8.5
Average	38	46.5	8.5

Figure 5.3 presents plots of middle and edge contour plots. The contour was taken from the edge of the rectangular ice block and compared with the middle. Because the maximum velocity occurred at the ice's surface flashing with the flume's center, the melt front of the ice taken from the edge differed slightly from that taken from the center of the ice geometry.

Table 5.3 Data comparison

Data	**Mean**	**SD**
Edge	33.26	8.25
Middle	31.66	8.23

The mean and standard deviation of the data set collected from the edge is 33.26 mm and 8.25 mm, respectively, while the middle contour plot data set has a mean of 31.66 mm and a standard deviation of 8.23 mm. Despite the broader data spread regarding the edge, there are no significant differences in their standard deviations. Hence, the successive contours were measured and traced from the ice's edge.

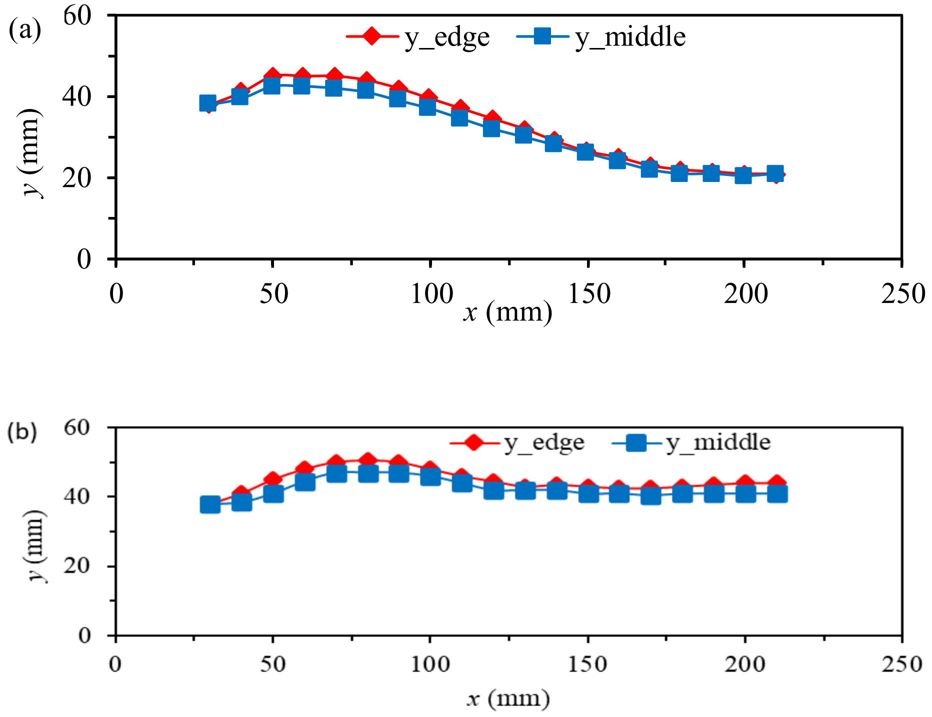

Figure 5.3 Edge and middle contour plot (a) sample 4 (b) sample 5

Experimental results for Re = 30147 are presented in Table 5.4. In Figure 5.4, the area below the curve represents the volume of ice that melts over time. On average, 50 mm of ice had dissolved from the side of the rectangular ice block perpendicular to the fluid flow direction. As shown in Table 5.4, the average scallop height is 12.3 mm, with trough positions ranging from 53.5 mm to 55 mm. The maximum scallop height was observed in Sample 1 to be 12.5 mm, while the lowest, 11 mm, occurred in Sample 5.

Table 5.4: Crest and trough positions; Reynolds number 30147

sample	**Crest (mm)**	**Trough position (mm)**	**Scallop height (mm)**
Sample 1	42.5	55.0	12.5
Sample 2	40.5	53.5	13.0
Sample 3	42.5	55.5	13.0
Sample 4	42.5	54.5	12.0
Sample 5	42.5	53.5	11.0
Average	42.1	54.4	12.3

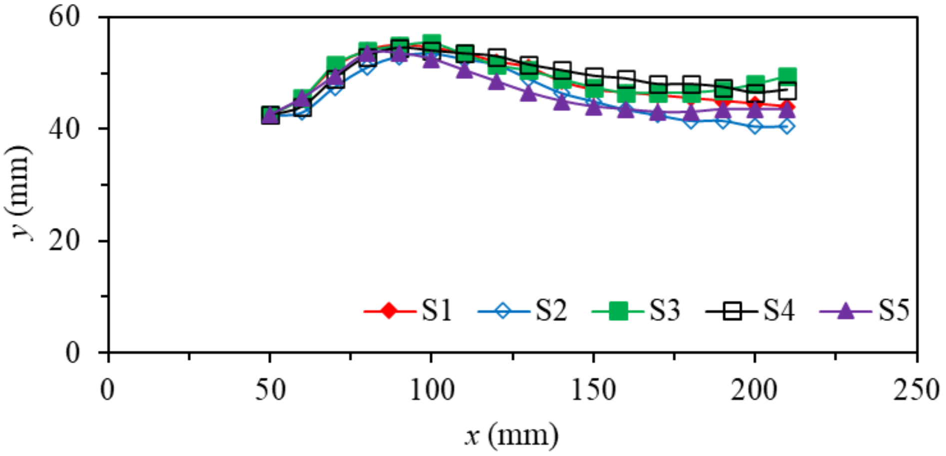

Figure 5.4 : Melt front of ice for Re = 30147

There are variations in melt rate moving from the leading edge through to the middle portion of the ice. The average basal melt recorded is 54.4 mm, observed in flow with Re = 30147.

The average contour plot is shown in Figure 5.5. Table 5.5 shows the conditions under which the test was conducted. The average initial ice temperature recorded was 9.18 °C, while the initial and final temperature of the ice and the water are presented for each sample in Table 5.5.

Table 5.5: Test Conditions, Re 30147

Test ID	$T_{initial\_water}$ (°C)	T_{final_water} (°C)	T_{ice} (°C)
T1$_{\text{-Re30147}}$	15.7	15.2	-12.3
T2$_{\text{-Re30147}}$	15.4	15.0	-9.0
T3$_{\text{-Re30147}}$	15.0	14.5	-7.5
T4$_{\text{-Re30147}}$	14.5	14.0	-8.2
T5$_{\text{- Re30147}}$	14.0	13.5	-8.9

The average contour plot is shown in Figure 5.5. Table 5.5 shows the conditions under which the test was conducted. The average initial ice temperature recorded was 9.18 °C, while the initial and final temperature of the ice and the water are presented for each sample in Table 5.5.

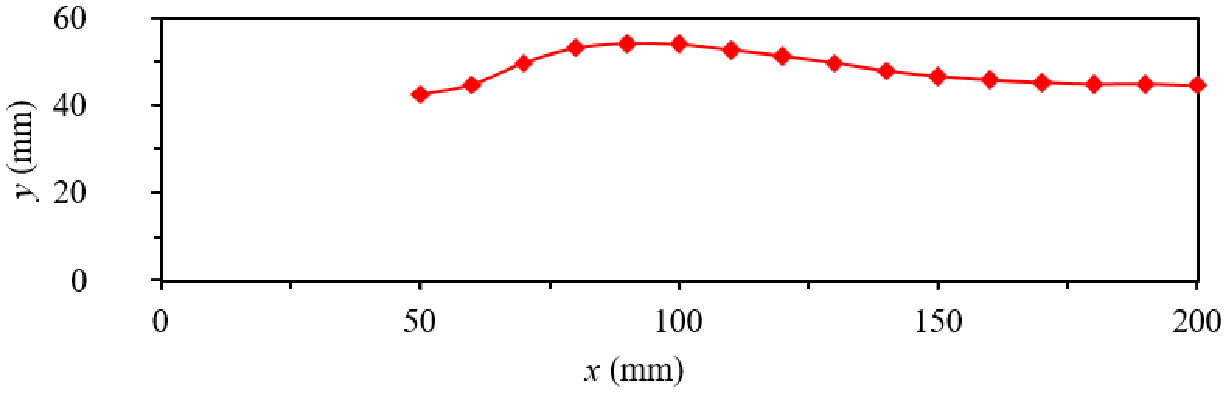

150 200

Figure 5.5: Average melt front for Re = 30147

Table 5.5: Test Conditions，Re 30147

Test ID	$T_{initial\_water}$ (°C)	T_{final_water} (°C)	T_{ice} (°C)
T1-Re30147-Tini-water15.7-Tice-12.3_	15.7	15.2	-12.3
T2-Re30147-Tini-water15.4-Tice-9_	15.4	15.0	-9.0
T3-Re30147-Tini-water15.0-Tice-7.5	15.0	14.5	-7.5
T4-Re30147-Tini-water14.5-Tice-10.1	14.5	14.0	-8.2
T5- Re30147-Tini-water14-Tice-8.9	14.0	13.5	-8.9

A total of five samples were tested with a flow of Re = 32768. The average basal melt recorded was 13.6 mm relative to the original block of ice. There are slight variations in the curves midway through to the tail end, as observed from the plot. The crest and trough positions are presented in

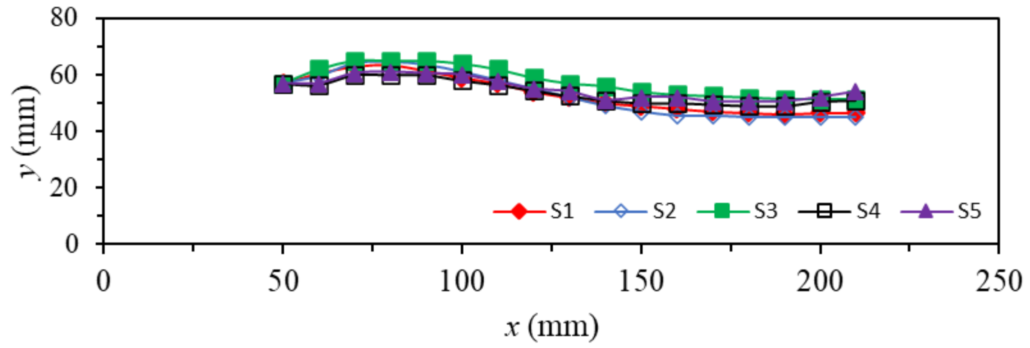

Figure 5.6: Melt front of ice for Re = 32147

Table 5.6: Scallop geometry

Sample	**crest (mm)**	**Trough (mm)**	**scallop height (mm)**
Sample 1	46	63.5	17.5
Sample 2	45	64.5	19.5
Sample 3	51.5	65	13.5
Sample 4	49	56.5	7.5
Sample 5	50.5	60.5	10
Average	48.4	62	13.6

Figure 5.7, on the other hand, illustrates the average contour plot of the five samples experimented.

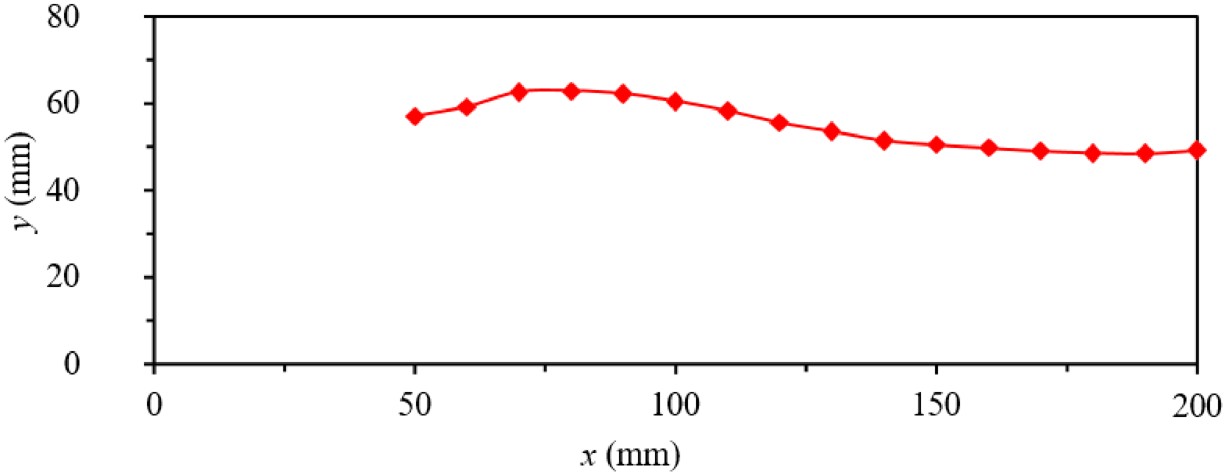

Figure 5.7: Average contour plot of melt front; Reynolds number 32768

5.2 Scallop Wavelength Effect

This section aims to investigate the effect of the Reynolds number on the wavelength of ice. Three different samples were tested under specific experimental conditions. Each experimental set was conducted for 15 minutes, during which scallop formation was observed. A fully developed scallop was formed within the test duration for the flow of Reynolds number 23265. The test was then run for an additional 5 minutes to ensure enough time for other scallops to develop, if any. No other scallop was formed as the first scallop ultimately evolved from a full scallop to less or no scallop. For the case of Reynolds number 30147, one fully developed scallop was observed at the leading edge within the test duration. A partial second feature had developed some distance from the first scallop but could not be classified as a fully developed scallop. However, the test for Reynolds number 32768 revealed two full scallops within the experimental time frame. The distance between the two scallops was measured, given a wavelength of 266 mm. Figures 5.8 and 5.9 show the images of the scallops.

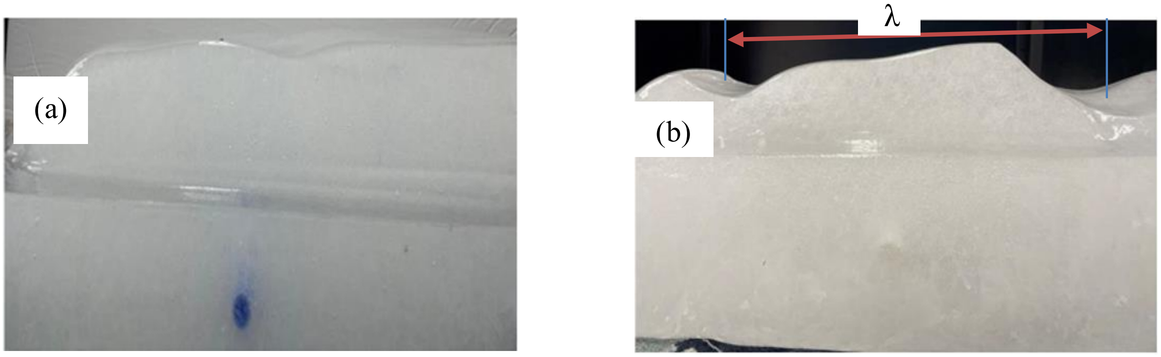

Figure 5.8 Scalloped ice (a) Re = 30147 (b) Re = 32768

An unexpected feature observed during the testing phase was the unexpected melting occurring at the left end of the rectangular ice block. The identified features developed are presented in Figure 5.9 with different views directions.

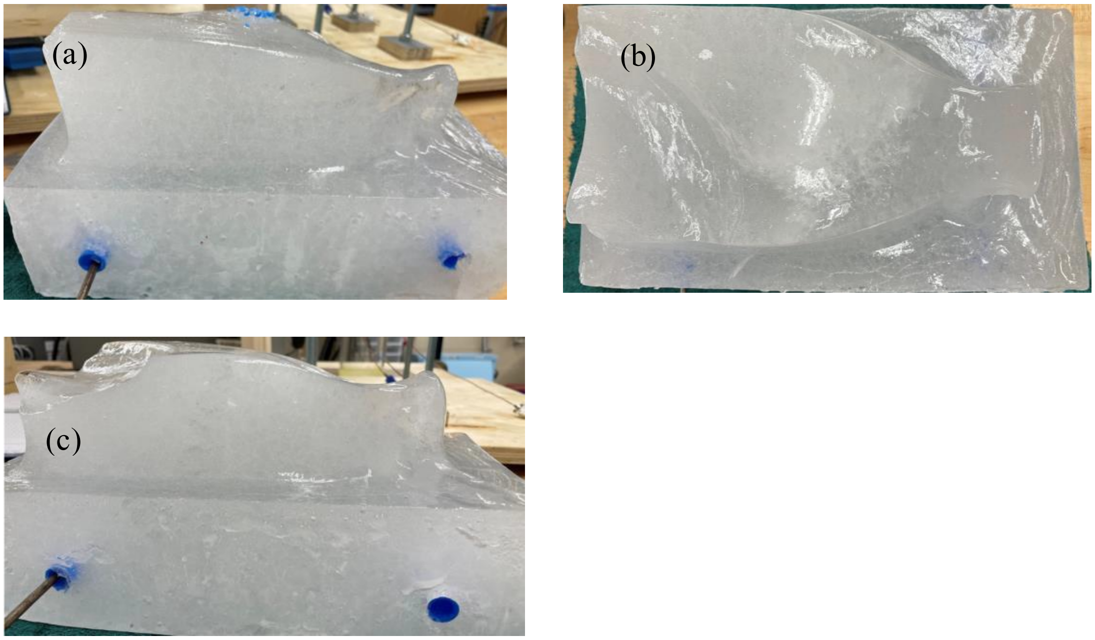

Figure 5.9: Partial surface melting of ice (a) right side view, (b) top view (c) left side

5.3 Change in Mass Effect

This section aims at finding the correlation between the Reynolds number and the melt rate of a rectangular ice block. Three different samples were tested under specific experimental test conditions presented in Table 5.7. The mass of each ice sample was measured before and after the experiment. The difference between the weights was taken and recorded. Table 5.7 shows that the flow with the highest Reynolds number recorded the highest melted mass corresponding to the mass difference of 5.470 lb, followed by a Reynolds number of 30147.

Table 5.7 Effect of Reynolds number on mass

Reynolds number	**Frequency (Hz)**	**T_{ice} (°C)**	**$M_{initial\_ice}$ (lb)**	**M_{final_ice} (lb)**	**Differences in mass (lb)**
23265	15	-10.4	17.00	11.94	5.060
30147	17	-9.7	17.46	11.99	5.468
32768	20	-10.1	16.45	10.98	5.470

5.4 Effect of Reynolds Number on Vertical Temperature Profile

Figure 5.10 shows a plot of spatial distance against the temperature profile from thermocouples embedded in a rectangular ice block 50 mm away from the leading front. The spatial distance between each thermocouple is 10 mm. The blue legend represents the vertical temperature profile across the ice. The initial temperature of the ice, $T_{ice\_initial}$, is represented by the orange code and has a temperature of -10.2 °C. The initial and final water temperatures were measured and recorded. The temperature profile from the plot varies between the initial ice temperature and the temperature of the water, represented by the "$T_{profile(front)}$" legend.

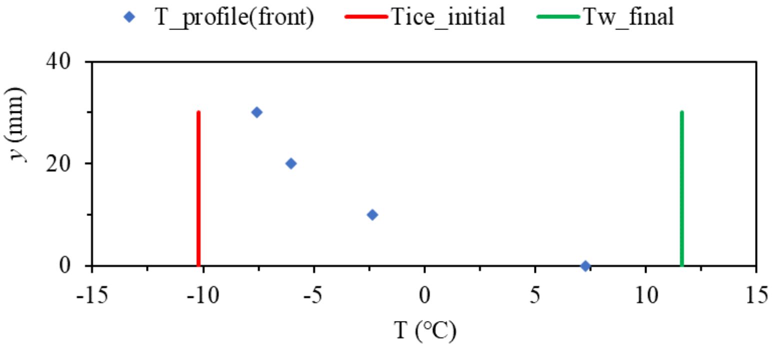

Figure 5.10: Temperature variation with spatial vertical distance (Leading front)

Figure 5.11, on the other hand, is a plot of the spatial distance against temperature with thermocouples embedded 50 mm to the left of the rear end of the ice. The lowest temperature recorded was -7.6 °C, which steadily reduced with reducing spatial distance. The experiment was conducted until all the thermocouples attained the temperature of the water in the flume. The highest temperature recorded was 6.4 °C, while the final temperature of the water was 12.9 °C.

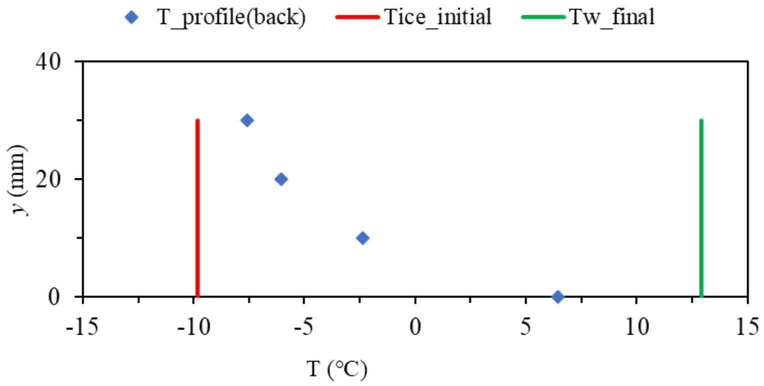

Figure 5.11 Temperature variation with spatial distance (Rear end)

5.5 Variation of Temperature with Time of the melting ice

Temperature variation of a melting rectangular ice block with time was investigated, and the results are presented in this section. The result shown in Figure 5.12 indicates the variation of temperature data collected from four thermocouple channels with time. The first thermocouple was positioned close to the surface of the rectangular ice block. Thermocouple 1 recorded a temperature reading of -4.2 °C at time 0 and steadily increased to 4.5 °C. In the third minute, the temperature drastically reduced to 3 (°C) from the previous reading due to the water-ice interface, thus the mushy zone. It increased steadily with time until it attained the highest temperature reading in the seventh minute. As expected, the other thermocouples recorded a steady increase in temperature as the ice melted with time. The experiment ended after all the thermocouples were exposed to water hence attaining the water temperature running through the flume.

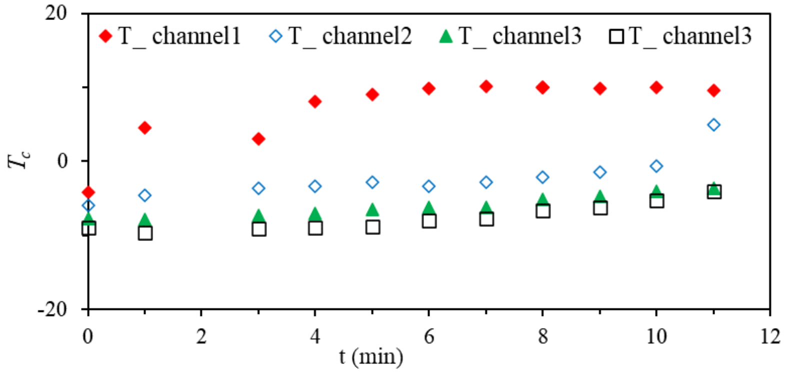

Figure 5.12 Variation of temperature with time (vertically arranged thermocouples)- rear end of the ice.

Table 5.7 Temperature readings with time (front)

Time (min)	T_{C1} (°C)	T_{C2} (°C)	T_{C3} (°C)	T_{C4} (°C)
0	-4.2	-5.9	-7.7	-8.9
1	4.5	-4.6	-7.9	-9.6
3	3	-3.7	-7.3	-9.1
4	8.1	-3.3	-7.0	-8.9
5	9	-2.8	-6.5	-8.8
6	9.9	-3.4	-6.2	-8.0
7	10.1	-2.8	-6.2	-7.7
8	9.9	-2.1	-5.2	-6.7
9	9.9	-1.5	-4.7	-6.2
10	10	-0.7	-4.1	-5.3
11	9.6	4.9	-3.6	-4.0

Figure 5.13 shows a temperature plot against time with thermocouples placed at 50 mm away from the leading front. Table 5.8 shows the temperature readings of the thermocouples with time.

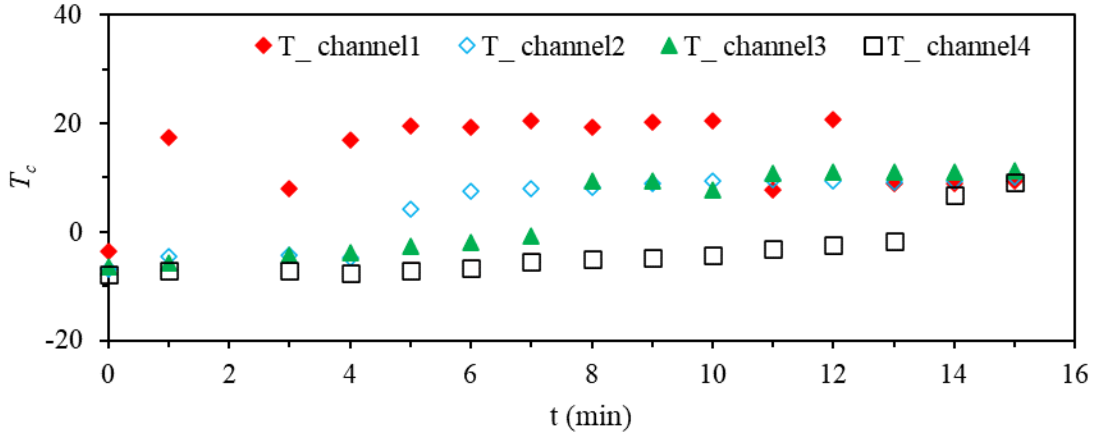

Figure 5.13: Temperature variation with time for vertically arranged thermocouples at the tail end of the rectangular ice block.

Table 5.8 Temperature readings with time (front)

Time (min)	**T_{c1} (°C)**	**T_{c2} (°C)**	**T_{c3} (°C)**	**T_{c4} (°C)**
0	-4.2	-5.9	-7.7	-8.9
1	4.5	-4.6	-7.9	-9.6
3	3.0	-3.7	-7.3	-9.1
4	8.1	-3.3	-7.0	-8.9
5	9.0	-2.8	-6.5	-8.8
6	9.9	-3.4	-6.2	-8.0
7	10.1	-2.8	-6.2	-7.7
8	9.9	-2.1	-5.2	-6.7
9	9.9	-1.5	-4.7	-6.2
10	10.0	-0.7	-4.1	-5.3
11	9.6	4.9	-3.6	-4.0

5.6 Effect of Reynolds Number on Temperature Profile along the Ice

The effect of the Reynolds number on the temperature profile along the rectangular ice sample was investigated, and the results are presented in this section. Six thermocouples were frozen into each ice sample 40mm away from the base of the ice and arranged horizontally. The distance between each thermocouple channel is 50 mm. Each test set was conducted until all the thermocouples fell into the water flowing through the rectangular flume.

5.6.1 Effect of Melting on Temperature Distribution

Table 5.9 shows temperature data collected with time for the flow of Re = 23265. The initial temperature of the ice was 11.1 °C, which was measured in the cold room before transferring the ice to the thermal research lab. The initial and post-experiment water temperature was recorded as 8.3 °C and 8.2 °C, respectively. The first thermocouple recorded a temperature of 0.3 °C; the next temperature recorded at 2 minutes increased rapidly to 9.1°C in Table 5.9 as the thermocouple became exposed to the water in the channel. Similarly, the five other thermocouples had a temperature reduction until they were exposed to water. It took an average of 28 minutes and 30 seconds for all the thermocouples to attain the water temperature as shown in Figure 5.14.

Table 5.9: Horizontal Temperature data: Re 23265

Time (min)	**T_{c1} (°C)**	**T_{c2} (°C)**	**T_{c3} (°C)**	**T_{c4} (°C)**	**T_{c5} (°C)**	**T_{c6} (°C)**
1	0.3	-9.2	-10.3	-9.7	-10.1	-10.1
2	9.1	-9.2	-10.4	-9.8	-10.1	-10.1
3	9.1	-8.1	-10.2	-9.1	-9.5	-9.8
4	9.0	-6.8	-9.7	-8.5	-8.7	-9.0
5	9.1	-5.1	-8.7	-7.4	-7.6	-7.9
6	9.1	-3.9	-7.9	-6.9	-6.9	-7.1
7	8.8	-3.1	-7.4	-6.3	-6.9	-6.7
8	8.8	-2.4	-6.8	-5.9	-6.2	-6.4
9	8.6	-1.5	-6.3	-5.2	-5.7	-6.0
10	8.6	-1.5	-5.9	-5	-5.2	-5.6
11	8.7	-0.7	-5.0	-4.2	-5.0	-5.1
12	8.8	-0.5	-4.4	-3.6	-4.5	-4.7
13	8.6	6.5	-3.5	-2.7	-4.0	-4.7
14	8.8	6.9	-2.8	-2.2	-3.5	-9.9
15	8.8	7.3	-2.3	-1.9	-2.9	-3.5
16	8.8	7.7	-1.4	-1.5	-2.4	-3.2
17	8.8	7.9	-0.6	-1.0	-2.0	-2.9
18	9.6	8.2	5.1	0.2	-1.2	-1.9
19	11.6	8.3	8.2	7.4	-1.0	-1.5
20	11.6	9.4	8.5	7.5	-0.2	-1.0
21	12.5	9.3	8.5	8.6	4.1	-0.8
22	12.8	10.2	9.3	9.1	5.2	-2.5
23	13.5	10.2	9.6	9.2	8.5	-2.4

Figure 5.14 presents plots of temperature variation with time for Re 23265, 30147, and 32768. The T_channel1 shows the temperature profile for the first thermocouple close to the ice samples' front edge. In Figure 5.14(a), there is a rapid increase in the temperature recorded for thermocouple1 as the initial location of the thermocouple had a film of ice covering the sensor. The rapid increase in temperature resulted from water exposure, hence attaining its temperature.

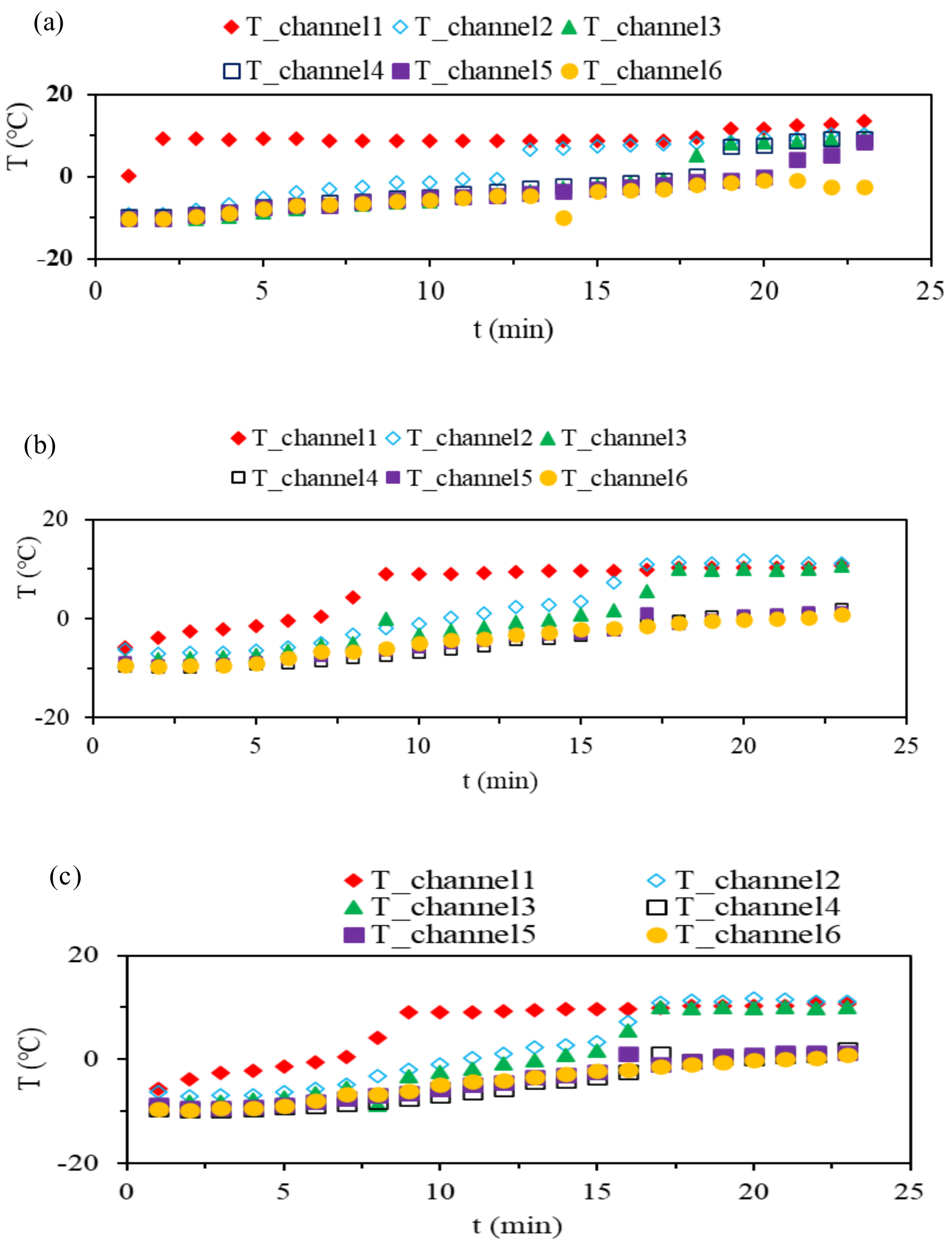

Figure 5.14: Horizontal Temperature profile (a) Re = 23265 (b) Re = 30147 (c) Re = 32768

The second thermocouple, T_channel2 recorded an initial temperature of -9.2 °C but less than the initial temperature of the ice. The successive temperature readings increased steadily until exposure to water. However, the sixth thermocouple, T_channel6 experienced a smooth transition from ice temperature to the attainment of water temperature.

5.6.1 Effect of Spatial Distance and Temperature on Melting

The effect of spatial distance on the temperature profile along the length of the ice was investigated, and results are presented as plots of spatial distance against temperature. The average temperature readings of each thermocouple outlet are computed and plotted against spatial distances for each thermocouple. Figure 5.15 shows the temperature profile plot for Re = 23265. The initial temperature of the ice, T_ice was 11.1 °C, while the final temperature of the water measured post-test was 8.3 °C. From the plot, the average temperature of the ice reduced from -5.33 gradually with time to 9.28 °C. Figure 5.15 shows a temperature plot against spatial distance with thermocouples arranged horizontally across the length of the ice sample. The results show a gradual drop in temperature reading from the leading edge to the tail end.

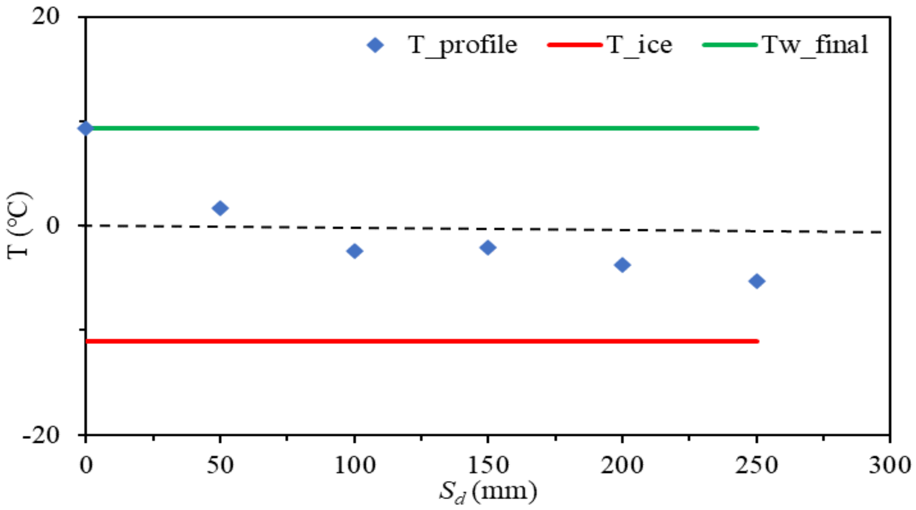

Figure 5.15: Spatial distance against Temperature, Re = 23265

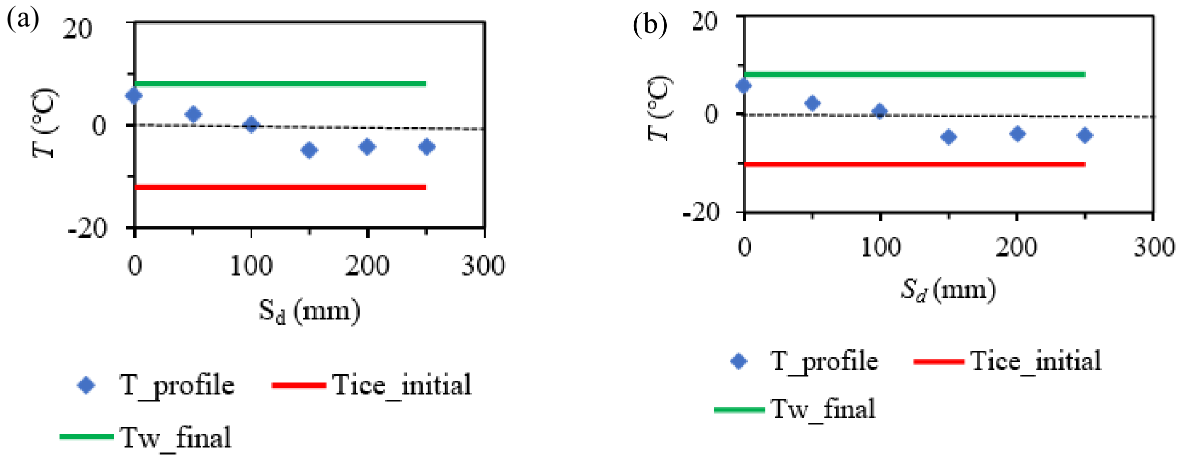

Figure 5.16: Spatial distance plotted against Temperature (a) Re 30147 (b) 32768

5.7 Numerical Result-Multiphase Flow

This section aims to validate the numerical model for water flowing through the channel. Profiles of streamwise velocity flow through an open channel are presented in this section. Figure 5.17 illustrates the logarithmic law profiles for the flow of Re = 23265, 30147, and 32768. The simulated data followed the logarithmic velocity profiles for Re = 23265 but slightly deviated in the case of Re = 32768.

However, there was simulated data located in the viscous and buffer regions of the linear and log law velocity profile plots.

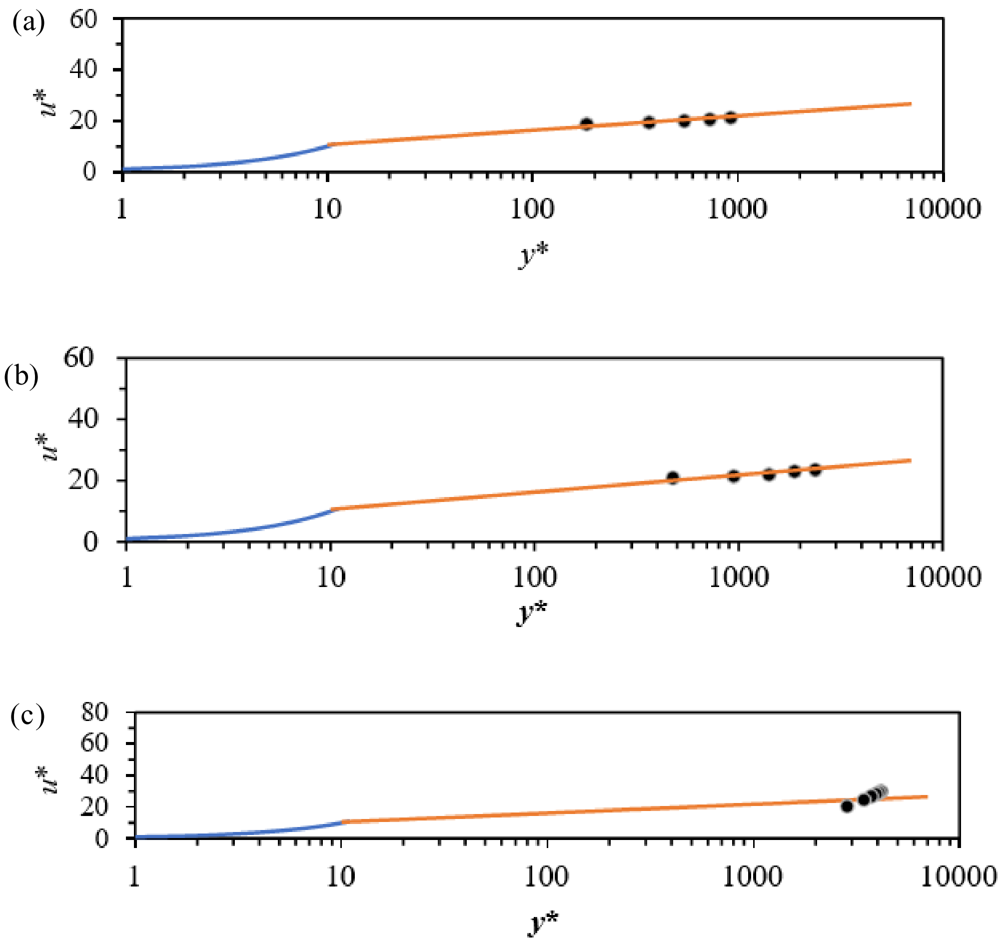

Figure 5.17: Logarithmic law velocity profiles; (a) Re = 23265 (b) Re = 30147 (c) Re = 32768

For Re = 32768, two data points are in the log-law region, while the rest are at the outer layer. Figure 5.18 shows the volume fraction and velocity contour plots. The point where the red and blue contours meet represents the interface between water and air. The solution diverted for Re of 32768 as floating points occurred above the computational domain. On the other hand, Figure 5.21 (c) shows a picture of the velocity contour plot for Re = 32768. Vortices are observed to have developed at the interfaces of water and air. Water is observed to have splashed out of the computational zone.

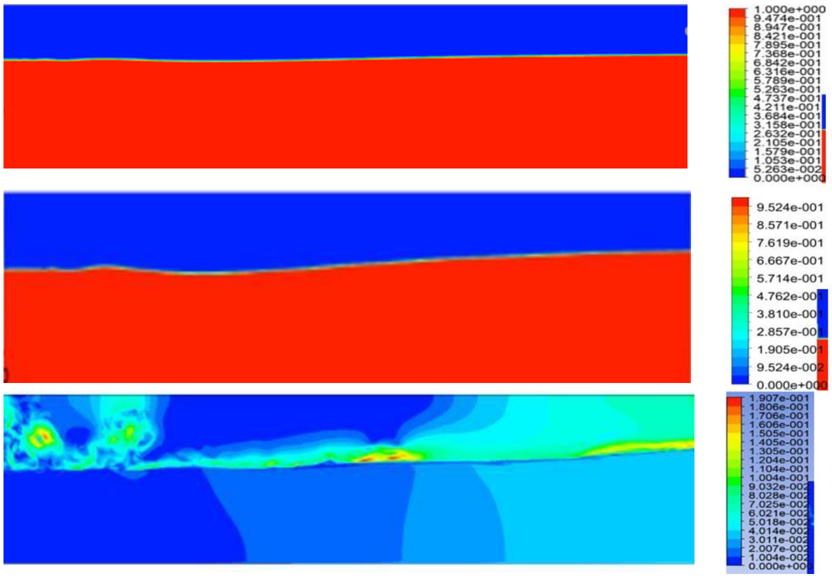

Figure 5.18: volume and velocity contours at t=10 min (a) volume fraction Re = 23265 (b) volume fraction Re = 30147 (c) velocity contour plot Re = 32768

5.8 Results for Enthalpy-Porosity Approach

This section aimed to simulate the formation of ice scallops numerically. The results of the simulation are presented in Figure 5.19. The investigation was carried out using the enthalpy-porosity method. First, a study was conducted to determine the appropriate mushy zone constant to incorporate into the simulation. A range of 10^5 to 10^7 of mushy zone constant was considered in the study. The volume average of liquid fraction is plotted and presented for $10^5, 10^6$ *and* 10^7 mushy zone constants in Figure 5.19. The computation domain was initialized at -10 °C. After applying a constant temperature input of 10 °C representing the initial average temperature of the fluid, the volume average of the liquid fraction of the mushy zone constant 10^5 rapidly increased to 0.0036.

In contrast, 10^6 zone constant had the initial highest volume average of the liquid fraction of 0.0042. The final volume average of liquid fraction for mushy zone constant 10^5 attained the highest volume fraction of the three-zone constants with a 60 s simulation time. The zone constants were used to simulate, and the result is shown in Figure 5.19.

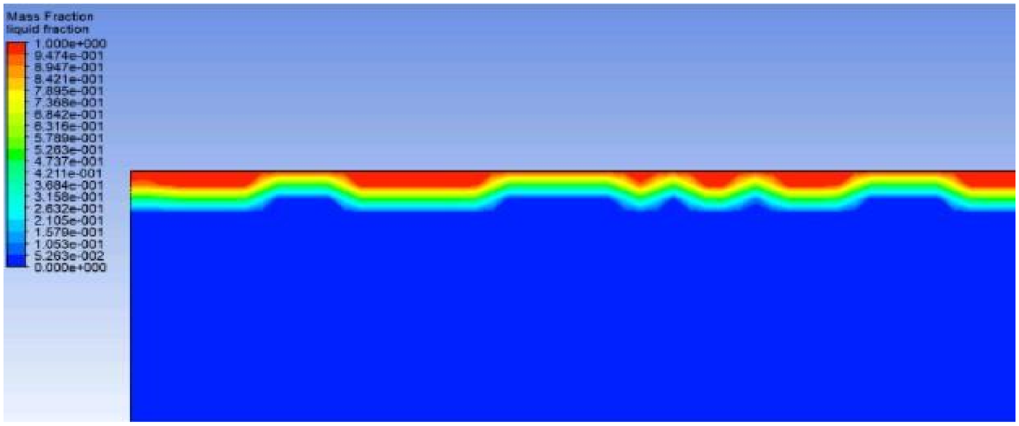

Figure 5.19 Scalloped ice with mushy zone constant 10^5

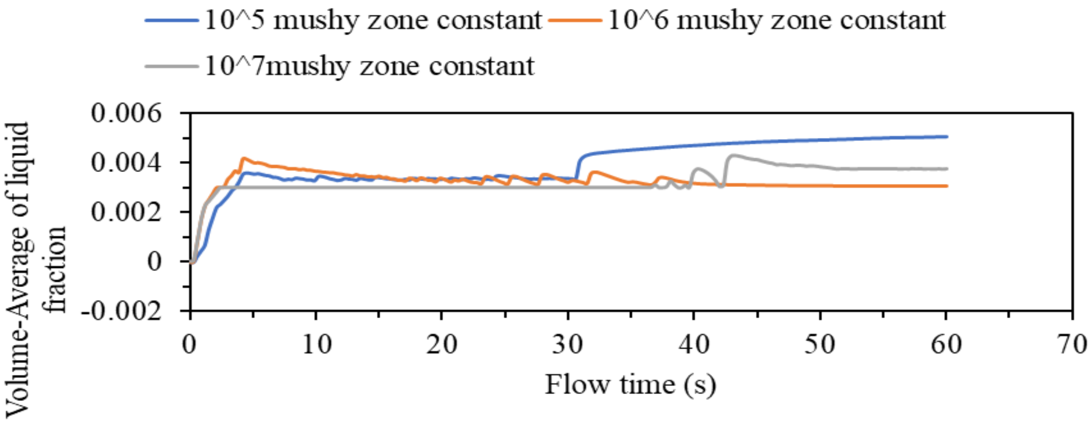

Figure 5.20: volume-average liquid fraction for mushy zone constants 10^5, $10^{6,}$ and 10^7

10^6 zone constant initially had the highest volume average of the liquid fraction, but it became constant when it reached 0.003. The zone constants 10^7 and 10^5 attained a higher liquid fraction after 30 seconds of flow time. Hence, the zone constant 10^5 was used to simulate the melting of the ice. After 30 seconds of flow time, there was enough water in the computational domain which resulted in changed in the heat transfer coefficient leading to the observed zig-zag in the curves. The mushy zone considered for the melting analysis is 10^5 as it leads to more volume of fluid in the computational domain. The volume of water reduces with increasing mushy zone constant.

5.9 Velocity Effect

Figure 5.21 shows the horizontal-velocity component contour plot for three Reynolds numbers, Re 23265, Re 30147, and Re 32768. The horizontal-velocity component contour plot in Figure 5.21(a) shows fluid separation immediately downstream of the ice's edge, resulting in a wake region. The maximum velocity is observed below the wake region as fluid slides the region at a magnitude between 0.6 – 0.7 m/s. The liquid separates and reattaches to the surfaces at a distance 0.17 m away from the origin of the ice. The fluid jets off in an axial direction at the tail end of the ice, while a reverse flow is indicated with dash lines at the top back of the ice close to the free surface. The lowest velocity occurred close to the surfaces of the ice at the leading edge, at the back of the ice, and in the wake region. The horizontal-velocity component contour plot for Re = 30147 and Re = 32768 showed similar features with a maximum velocity of 0.7 to 0.8 m/s and 0.8m/s, respectively. The maximum velocity under the wake region increases with increasing Reynolds number, as observed in Figure 5.21. The point of reattachment is observed to increase with increasing Reynolds number, similar to the size of the reverse flow.

Figure 5.22, on the other hand, presents contour plots of the vertical component velocity for Re = 23265, Re = 30147, and Re = 32768. The highest vertical-velocity component appears behind the reverse flow region and increases with increasing Reynolds number. The vertical-velocity component beneath the ice region is observed to have a y-component velocity between (0 – 0.1) m/s. According to the contour plot, the highest vertical-velocity component is estimated at 0.39 m/s. From Figures 5.22 (a), (b), and (c), the lowest vertical-component velocity is experienced at the bottom leading edge of the ice. Reverse flow occurred at the bottom leading edge, and the size is seen to increase with increasing Reynolds number.

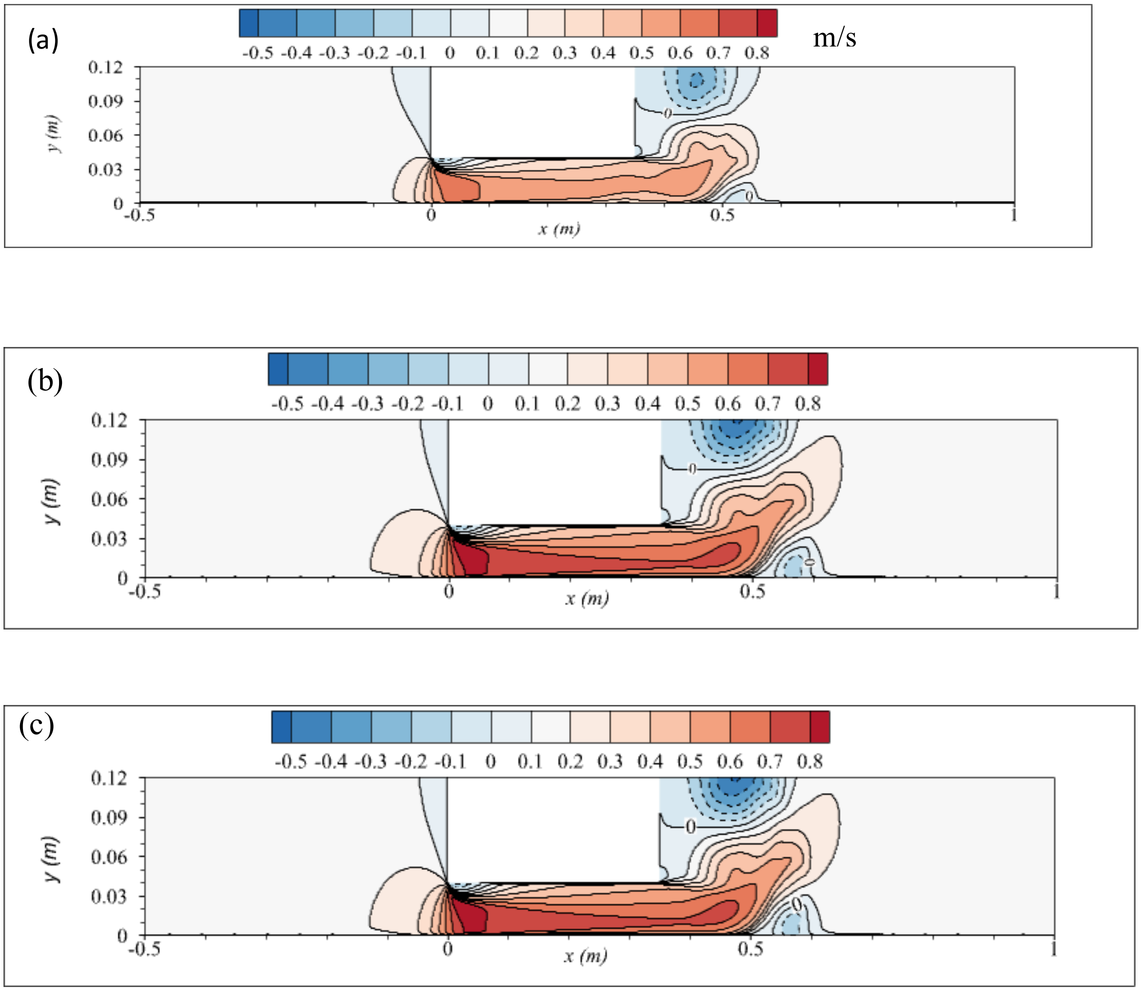

Figure 5.21: Horizontal velocity component plot (a) Re = 23265 (b) Re = 30147 (c) Re = 32768

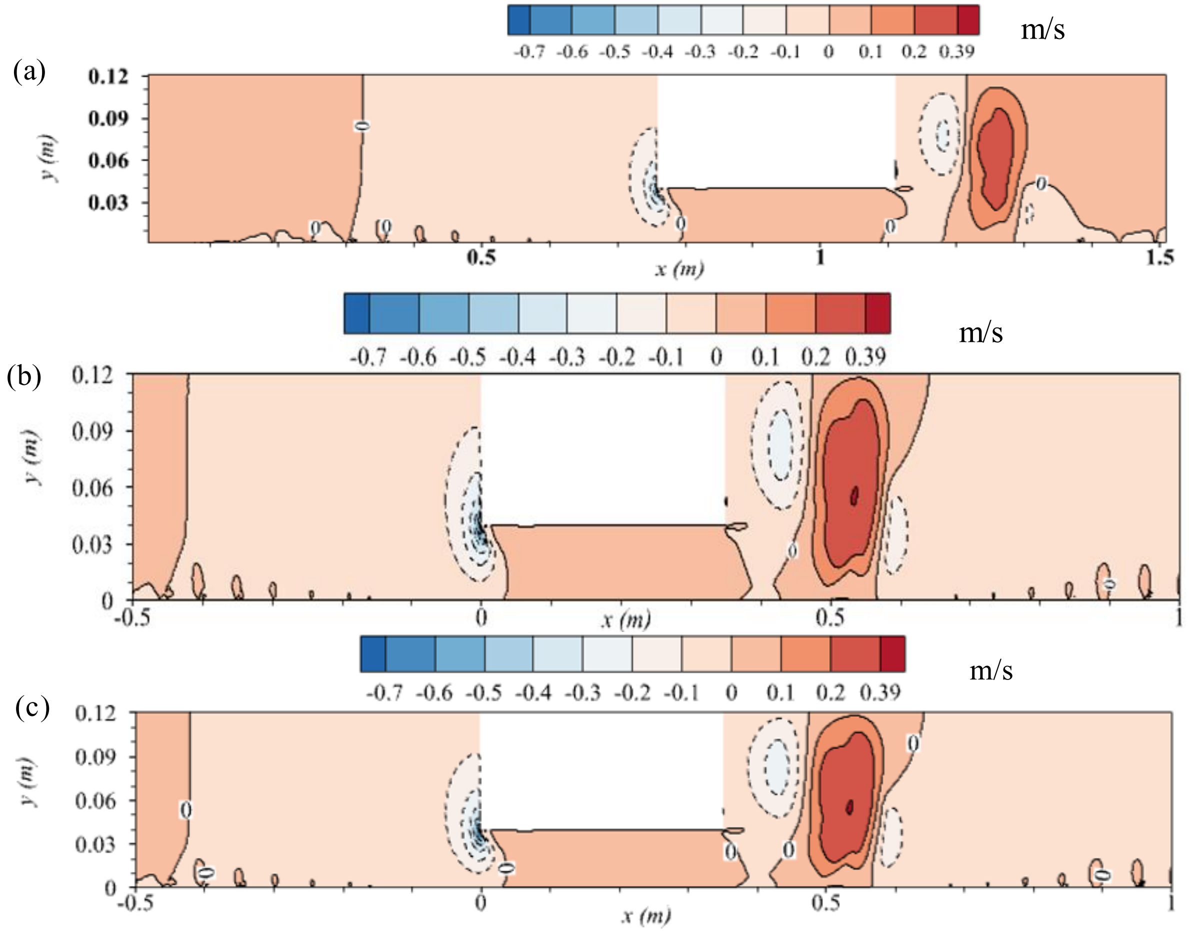

Figure 5.22: Vertical velocity component plot (a) Re = 23265 (b) Re = 30147 (c) Re = 32768

Figure 5.23 shows contour plots of the horizontal velocity component of a simulated scalloped ice geometry with Reynolds numbers 23265, 30147, and 32768. The horizontal velocity is observed to be lowest at the region of the fluid separation and behind the simulated ice. In contrast, the maximum velocity is recorded away from the wake layer, and the maximum velocity increases with increasing Reynolds number.

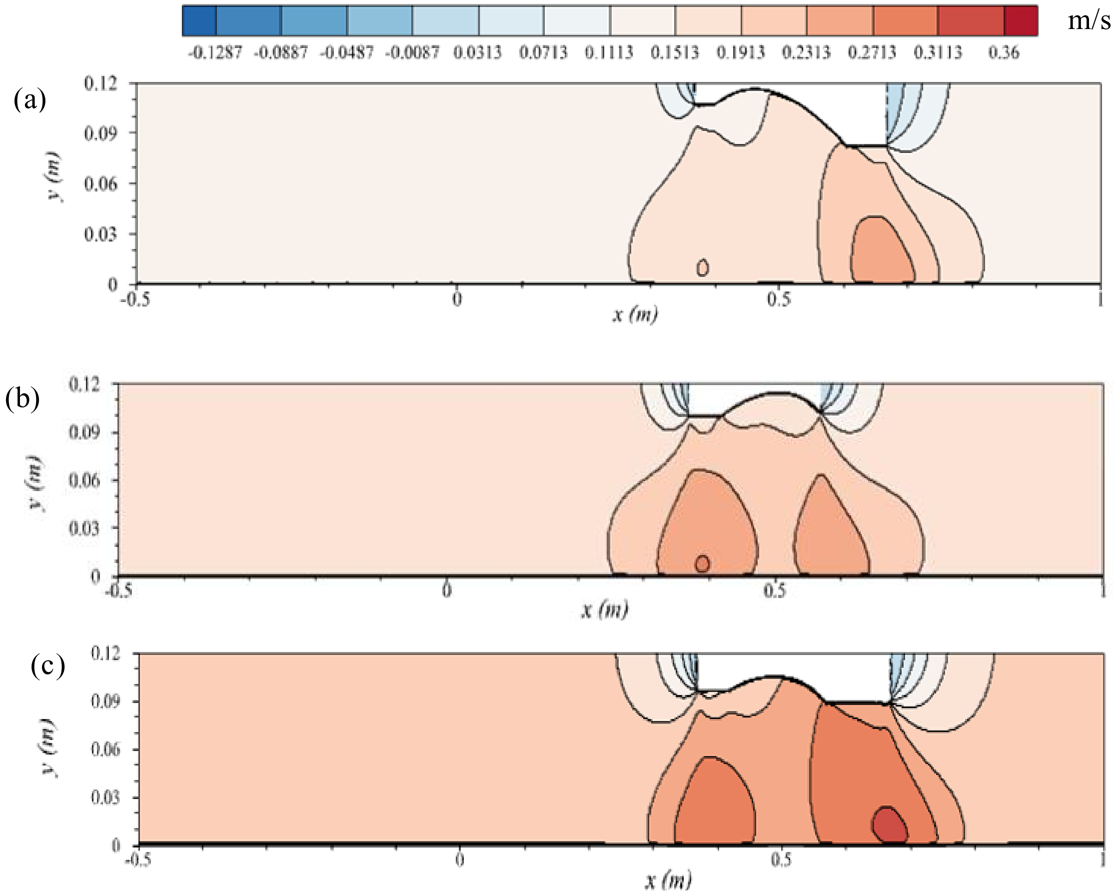

Figure 5.23 Horizontal velocity on scallop region (a) Re = 23265 (b) Re = 30147 (c) Re = 32768

5.10 Pressure Effect

The effect of fluid pressure on scallop formation is investigated via a numerical approach using commercial software, and results are presented in this section. Figure 5.24 represents the pressure contour plots for different Reynolds numbers. The pressure at the inlet and the leading edge of the ice is observed to have increased with increasing Reynolds number. The inlet pressure for Re 23265 varies between 113 – 135 Pa, while Re = 30147 and Re = 32768 vary between 179 -193 Pa and 193 – 232 Pa, respectively.

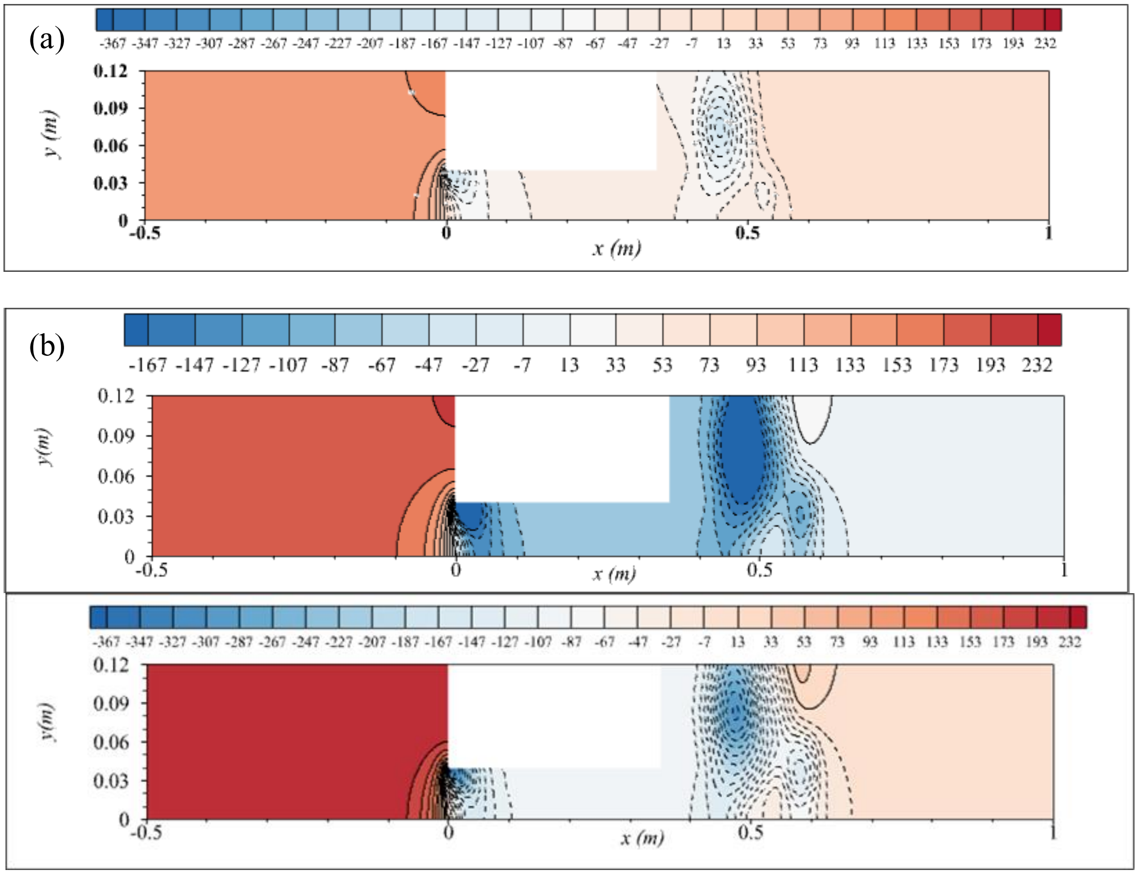

Figure 5.24: Pressure contour plot (a) Re = 23265 (b) Re = 30147 (c) Re = 32768

The bottom edge of the leading front of the ice experiences a drastic change in pressure as the fluid encounters the surface of the ice. As observed from the contour plot, negative pressure occurs at the wake region and within regions of the fluid flow reversal.

5.11 Temperature Effect

The temperature plot of the simulated domain is presented to widen the understanding of how temperature distribution affects the differential melting of the ice.

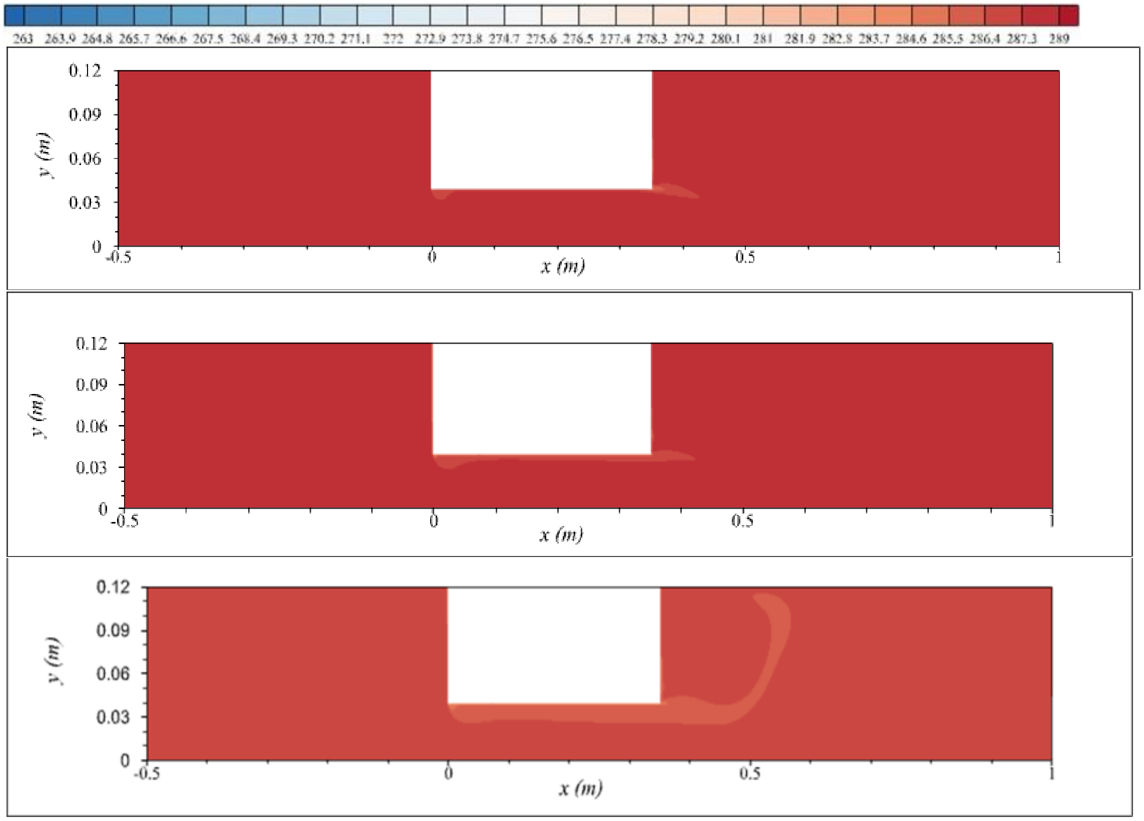

Figure 5.25: Temperature contour plot (a)Re = 23265 (b) Re = 30147 (c) Re = 32768

Figure 5.25 shows a contour plot of the temperature distribution across the domain. From the contour plot, it is observed that there is an uneven temperature distribution, resulting in the differential melt across the surfaces of the ice. The wake regions are seen to have lesser temperatures carrying fluid than other ice surfaces. The temperature at the point of reattachment of the water is higher than that of the wake region.

5.12 Velocity Profiles

The velocity profiles at specific locations in the flume and on the ice were considered and extracted for analysis. Figure 5.26 shows plots of the velocity profiles at different locations in the channel and around the ice. Figure 5.26 (a) shows the velocity profile for the flow of Re = 23265 at x = -0.5 m, Figure 5.26(b) shows the velocity profile x = 0.1 m, while the positions 0.25 m and 0.4 m and 0.8 m correspond to Figure 5.26 (c), (d), and (e) respectively. The maximum velocity in Figure 5.26 (a) is 0.3 m/s, corresponding to the velocity profile of the open water location. The velocity was 0 m/s at the boundary, steadily increasing until it reached maximum velocity. Figure 5.26 (d), on the other hand, has a velocity of 0 m/s close to the wall of the channel and that of the ice, given its shape. The velocity is observed to peak midway between the surface of the ice and the walls of the channel and is recorded as 0.56 m/s. Figure 5.26 (e) corresponds to the location at the back of the ice where the water surface is open to the air. The velocity profile at this location appears to be tapered and extends to the negative axis of the chart. The maximum velocity attained at this position is 0.33 m/s, while the lowest was -0.01 m/s. The velocity in the negative regions indicates a reverse flow.

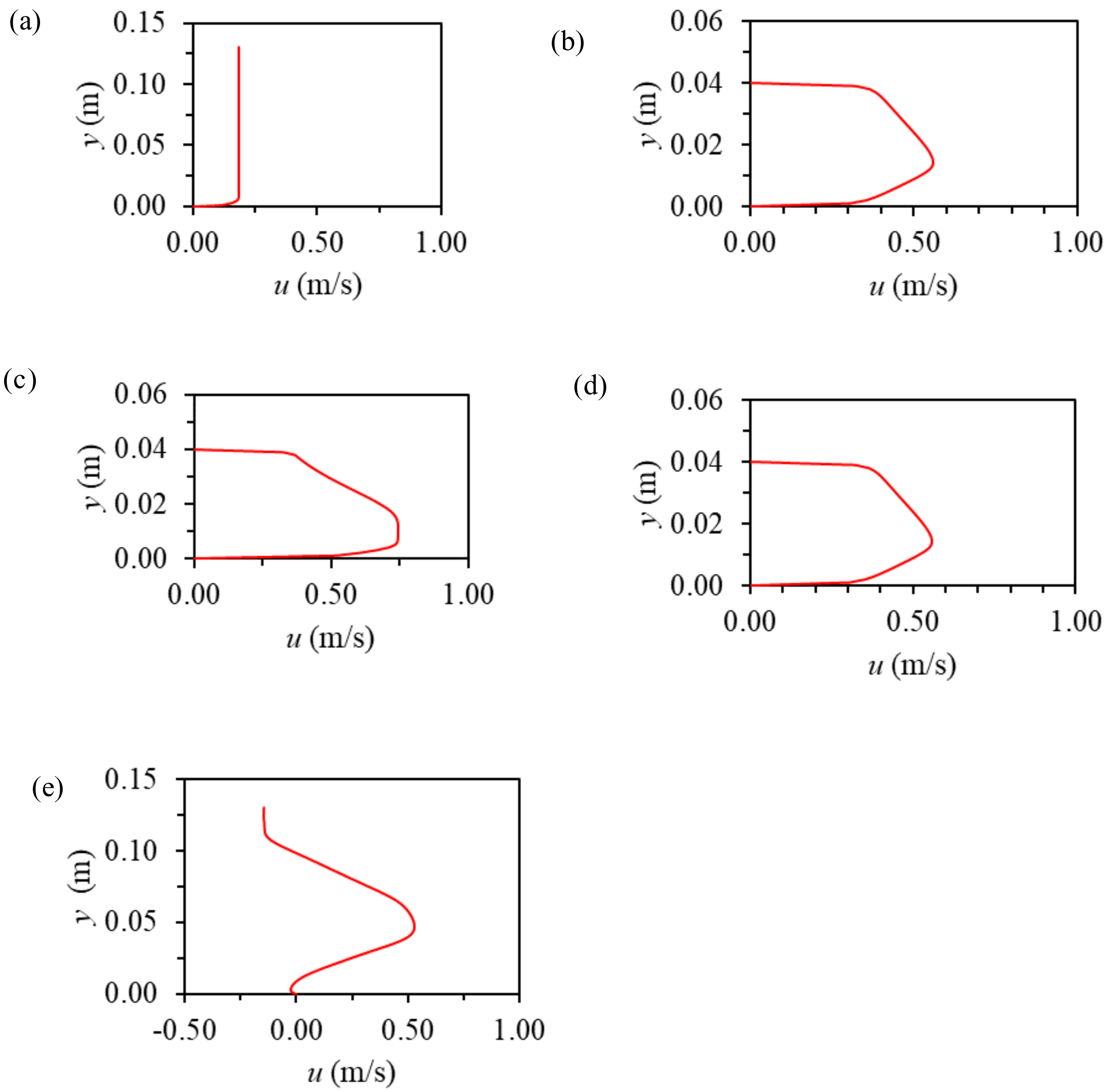

Figure 5.26: Velocity profile Re 23265 (a) x = -0.5 m (b) x = 0.1 m (c) x = 0.25 m (d) x = 0.4 m (e) x = 0.8 m

Figure 5.27 represents velocity profiles for the flow of Re = 30147 at specified locations. In Figure 5.27a, the flow attained a maximum velocity of 0.19 m/s away from the wall before it became constant. The profile extracted at x = 0.1 m is the velocity profile near the leading edge of the block of ice. The maximum velocity recorded was 0.81 m/s, while 0 m/s velocity was observed at the wall.

The graph shows a reverse flow close to the surface of the ice in contact with the water. Like the velocity profiles in Figure 5.30c, d, and (e) of Re = 23265, Re 30147 has similar profiles despite the differences in the profile because of differences in inlet velocity to the channel. The maximum velocities in Figure 5.27(c), (d), and (e) are 0.74 m/s, 0.72 m/s, and 0.53 m/s, respectively.

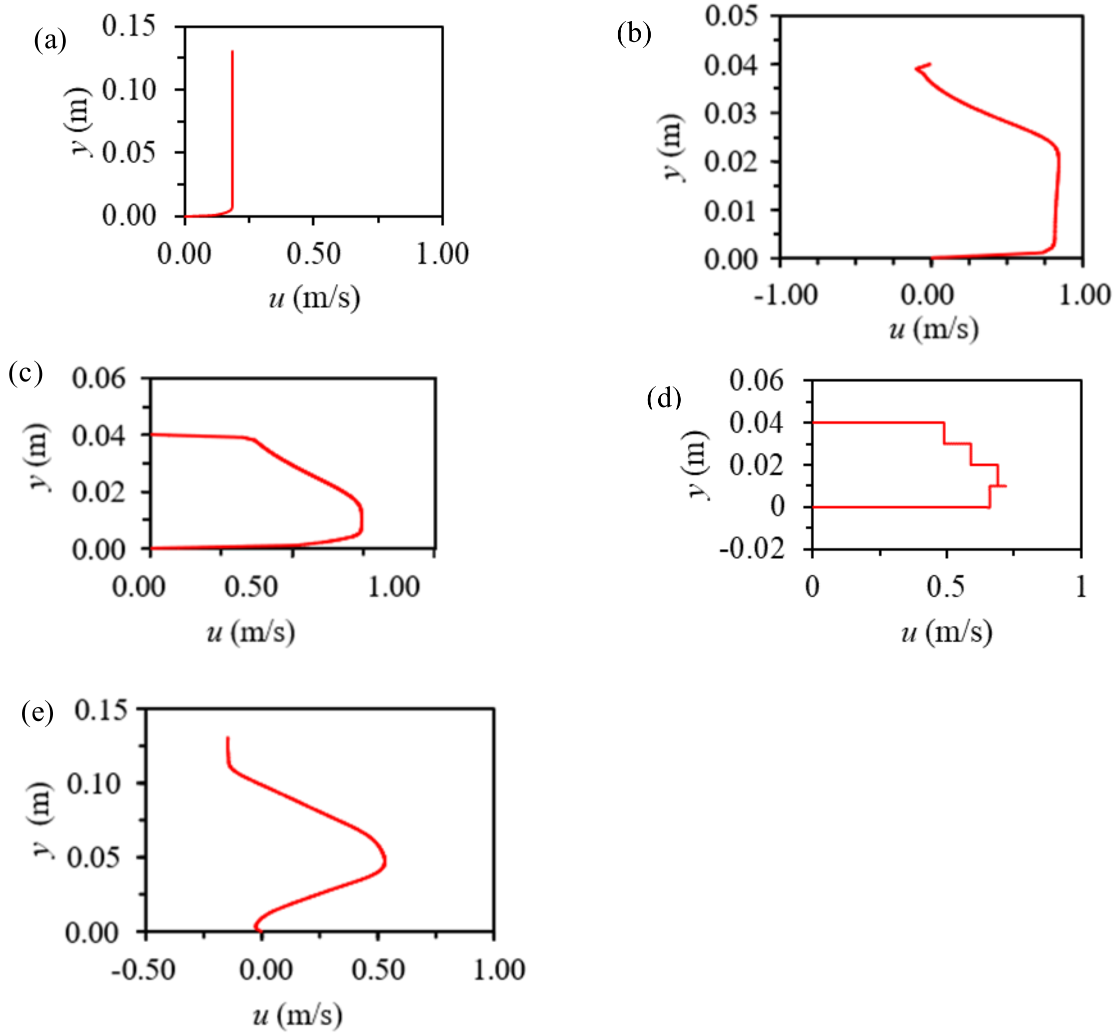

Figure 5.27: Velocity profile: Re 30147 (a) x = -0.5 m (b) x = 0.1 (c) x = 0.25 (d) x = 0.4 (e) x = 0.8m

Chapter 6: Analysis and Discussion of Results

6.1 Overview

In this chapter, results are presented and analyzed for comparison. The results are discussed, taking into consideration scientific principles for a deductive conclusion. The effect of the various parameters on scallop formation is presented and discussed in detail. The key parameters include the impact of the Reynolds number on the melting ice's melt rate and temperature profile. The effect of Reynolds number on the wavelength of scalloped ice is also discussed. To better understand and explain the phenomenon leading to the formation of ice scallops, numerical data on simulated ice is extracted from the model. Deductions are also made from video recordings taken during the experiment.

6.1.1 Effect of Reynolds Number on the Melting Process

The experiment revealed three stages of scallop formation: initial flat ice, intermediate scallop to fully developed scallop, and an evolving scallop geometry. The test was categorized into possible parameters contributing to the formation of ice scallops; the effect of three Reynolds numbers on the melt rate was investigated, and the results are presented and discussed in this section. Figure 6.1 illustrates the contour plots of the flow of Reynolds numbers 23265, 30147, and 32768. The melt rate differs with respect to each Reynolds number, as shown in Figure 6.1. The area under the curve indicates the amount of ice that had melted over the experimental time frame. The flow of Re 32768 has a higher melt rate, followed by Re 30147. The lowest melt rate was observed to have occurred with regard to Re 23265. The surfaces of the ice perpendicular to the direction of flow of the liquid experienced a higher melt rate than the basal and lateral melt.

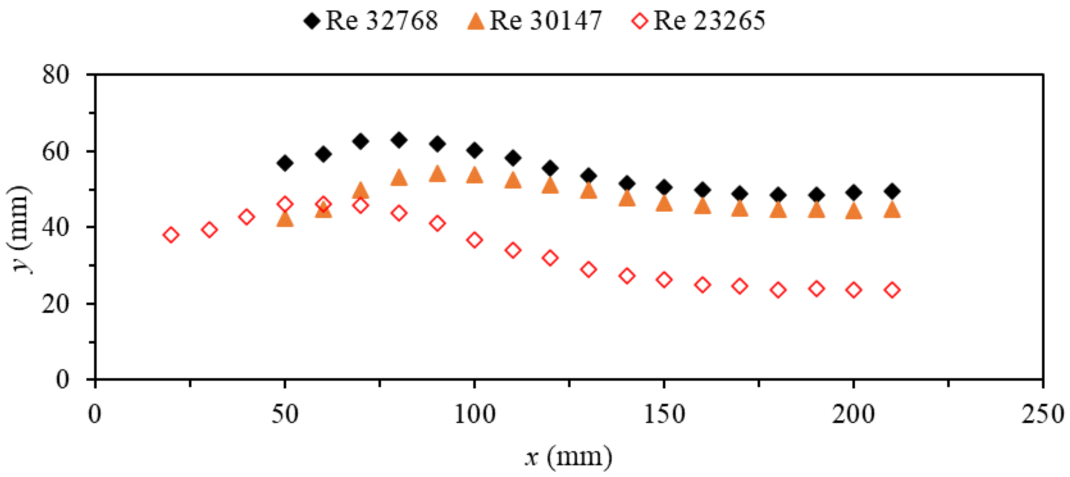

Figure 6.1: Comparison of the melt front; Re = 23265, 30147, and 32768

As the Reynolds number increases, more water gets pushed around the surfaces of the ice in 3-dimensional directions. With an initial velocity, the water hits the surfaces perpendicular to the flow direction, leaving a vertical fluid component. The shear velocity components contribute to the rapid heat exchange between the fluid and the ice surfaces perpendicular to the direction of the liquid. The fluid separates at the rectangular ice block's edge and re-attaches along the lateral length of the rectangular block. The size, strength of the vortices, and re-attachment point depend on the Reynolds number. Figure 6.2 shows the fluid molecules' attachment on the ice block's surfaces.

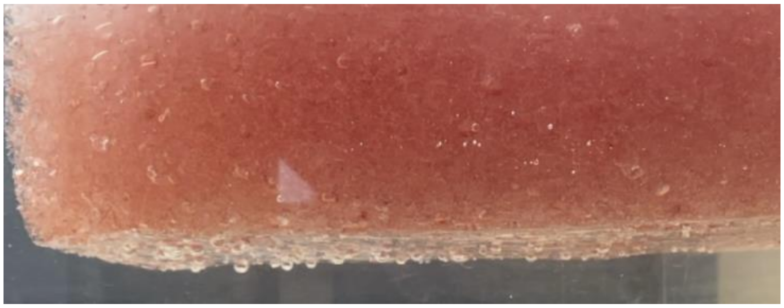

Figure 6.2: Attachment of fluid molecules on ice surfaces

Water molecules can be seen attached to the surfaces of the ice, while some liquid components slide along the ice surface with time.

6.1.2 Effect of Reynolds Number on Scallop Wavelength

This section presents an analysis of the wavelength of scalloped ice and the correlation between the Reynolds number and wavelength. As presented in the previous section, no additional visible scallop was developed within the 15-minute time frame for the flow of Reynolds number = 23265. One scallop was formed at the edge of the sample but evolved with time. For the case of Re = 30147, the first scallop was fully developed and equally evolved, while some partially formed scallops along the length of the sample could not be classified as full-blown scallops. Re of 32768 revealed two scallops, and the wavelength was determined. The higher the Reynolds number, the faster the deterioration of the leading edge. In addition, the flow of Reynolds number 32768 had the first scallop evolve more quickly from a fully developed scallop, followed by the vortex's progression and subsequent reattachment along the surfaces of the ice.

Similarly, the area under the curve in Figure 6.1 represents the amount of ice that melted over the duration, which is highest for Re = 32768 and lowest for Re = 23265. This indicates that the melt rate increases with increasing Reynolds number. The frontal melt rate for Re = 23265 was the lowest. Simultaneously, the rate of progression of vortical structures and subsequent re-attachment of flow separation was equally low, preventing the formation of a second scallop downstream of the ice block. However, for Re = 32768, the frontal melt rate was relatively higher, coupled with the transport of turbulent structures and re-attachment, forming a second scallop.

6.2 Effect of Temperature on Melting

The effect of temperature cannot be overlooked as it directly impacts the melt rate of the rectangular ice. The plot of the average temperature for each thermocouple channel against time is presented in Figure 6.3. From Figure 6.4, the average temperature gathered from each thermocouple with respect to each Reynolds number increases steadily from the initial average ice temperature to attain the temperature of water flowing through the channel with time.

The ice's melt rate for Re 32768 is higher, as it took 19 minutes for all the thermocouples to attain the flume water temperature. Re of 23265 has the lowest melt rate with a melt time of 28 minutes 30 seconds, as shown in Figure 6.3.

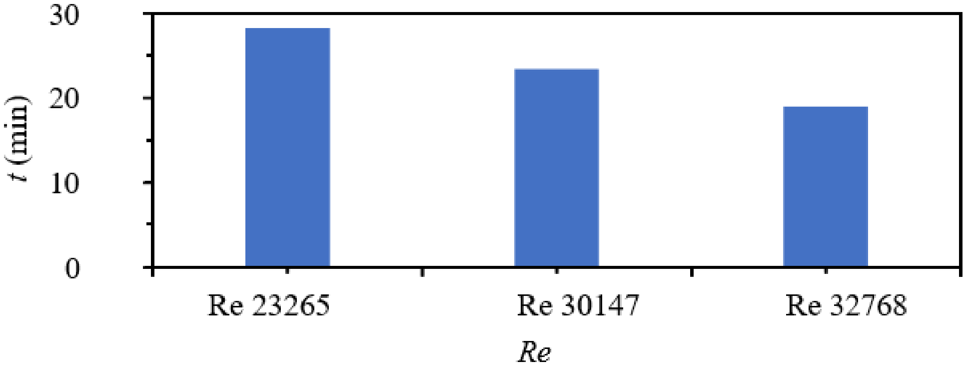

Figure 6.3: Melt rate as a function of Reynolds number

According to Figure 6.4, the order of the temperature profile changed mid-way from one Reynolds number to the other as the shape of the melting front of the ice determines the profile.

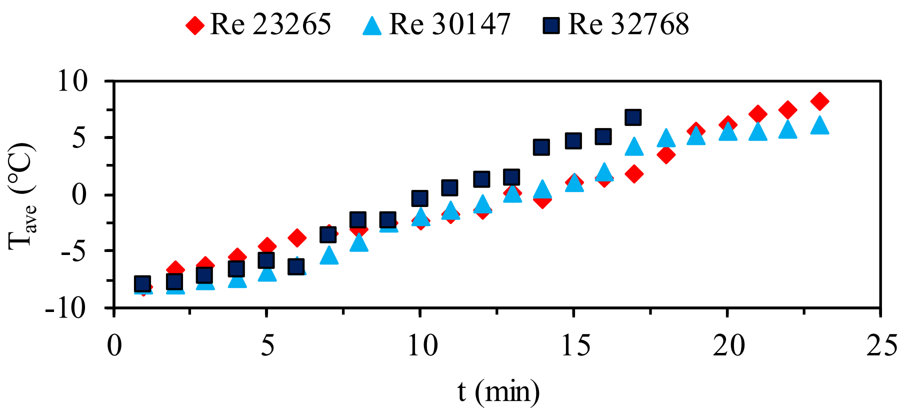

Figure 6.4: Temperature variation with time for Re = 23265, 30147, and 32768

Figure 6.5, on the other hand, shows the spatial distance plotted against the average temperature of ice. The temperature profiles with regard to each Reynolds number are compared with spatial distance. According to the temperature data collected, the ice's temperature decreases from left to right of the rectangular ice block as heat. Heat is transferred from the water to the ice via conduction while the remaining are transported along the channel. Moreover, the surface perpendicular to the direction of the water was observed to have the highest melt rate.

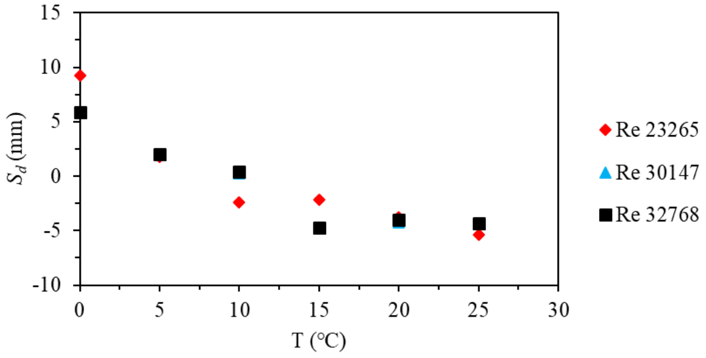

Figure 6.5 Spatial distance plot against temperature for Re = 23265 30147and 32768

Figures 6.6 and 6.7 are temperature distribution plots for different Reynolds numbers at different time intervals. The temperature distribution for the first thermocouple is displayed in Figure 6.6a (T1_Re 23265), and that of thermocouple channel 2 is displayed in Figure 6.6b. In Figure 6.6a, the initial temperature recorded for channel one is observed to be higher than the temperature data recorded for other thermocouple channels because the first sensor was closer to the surface of the ice than the other thermocouples giving rise to the observed abrupt rise in temperature. Figures 6.6 and 6.7 show a linear relationship between the time and temperature of the ice; hence, melting increases with increasing temperature of the working fluid.

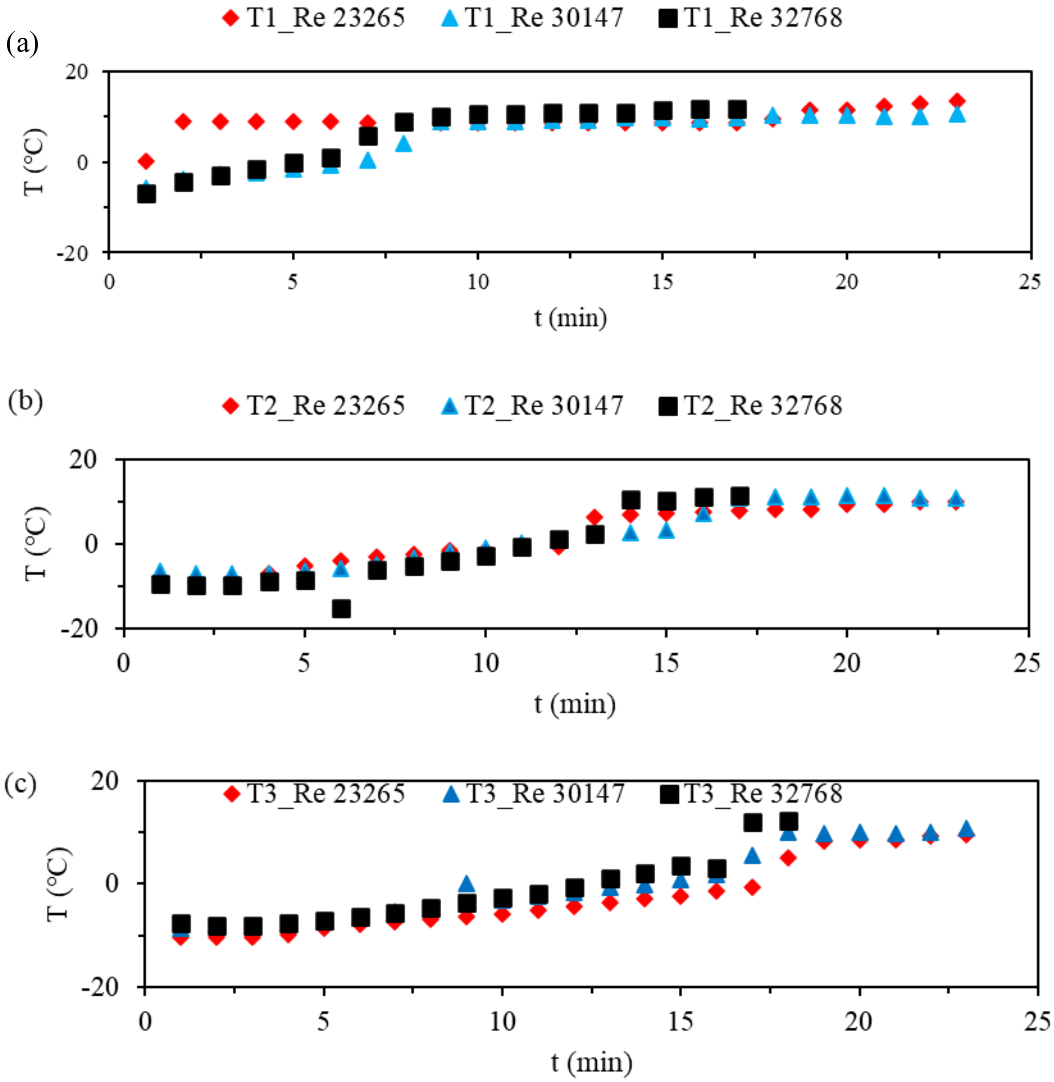

Figure 6.6: Temperature profiles (a) thermocouple channel 1 (b) thermocouple channel 2 (c) thermocouple channel 3

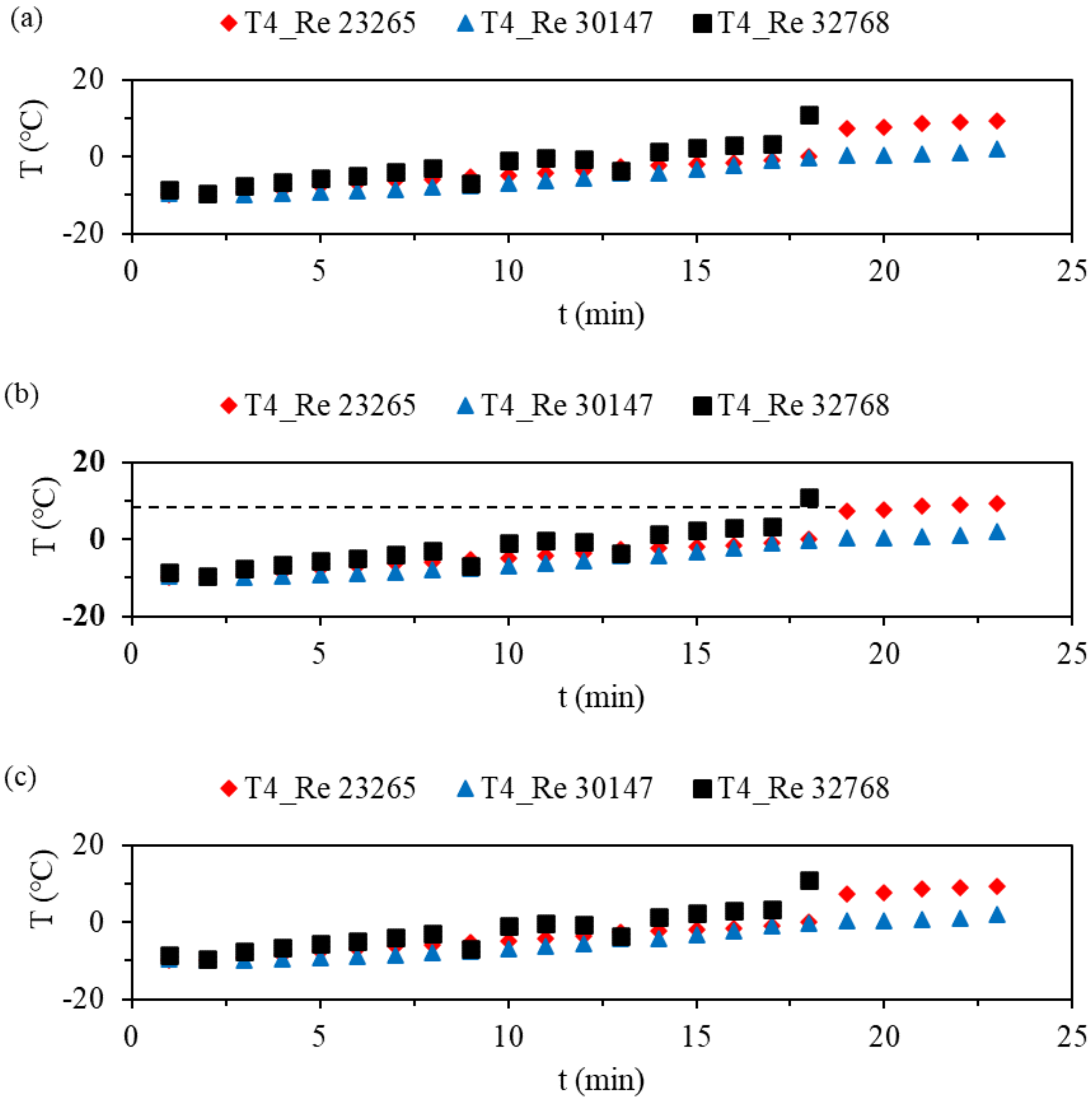

Figure 6.7: Temperature profiles (a) thermocouple channel 4 (b) thermocouple channel 5 (c) thermocouple channel 6

In Figure 6.7a, the first thermocouple channel is observed to have a different profile from the other channels because the initial position of the sensor was closest to the surface of the ice. The sensor was exposed to water, hence the abrupt temperature change recorded by the sensor. The initial profile of the plots in Figure 6.7 are linear until the sensors were exposed to water, leading to a significant change in temperature reading.

6.3 Time Series of Evolving Ice Geometry

Figure 6.8 shows the time series of the evolving ice. The ice sample was initially flat at zero minutes, with a velocity boundary layer developing at the ice-water interface. The ice experienced a non-uniform basal and frontal melting in the second minute, as shown in the figure below. The frontal rate of melt is observed to be higher than the basal melt rate as the front is perpendicular to the water's flow direction. A fully developed scallop is observed in the sixth minute. The progression of the scalloped ice from fully formed ice started in the eighth minute. In the tenth minute, the fully developed scallop is seen to have reduced in size and geometry. Basal melting occurs as a result of turbulence action, and differential melting is caused by the separation and reattachment of vortical structures.

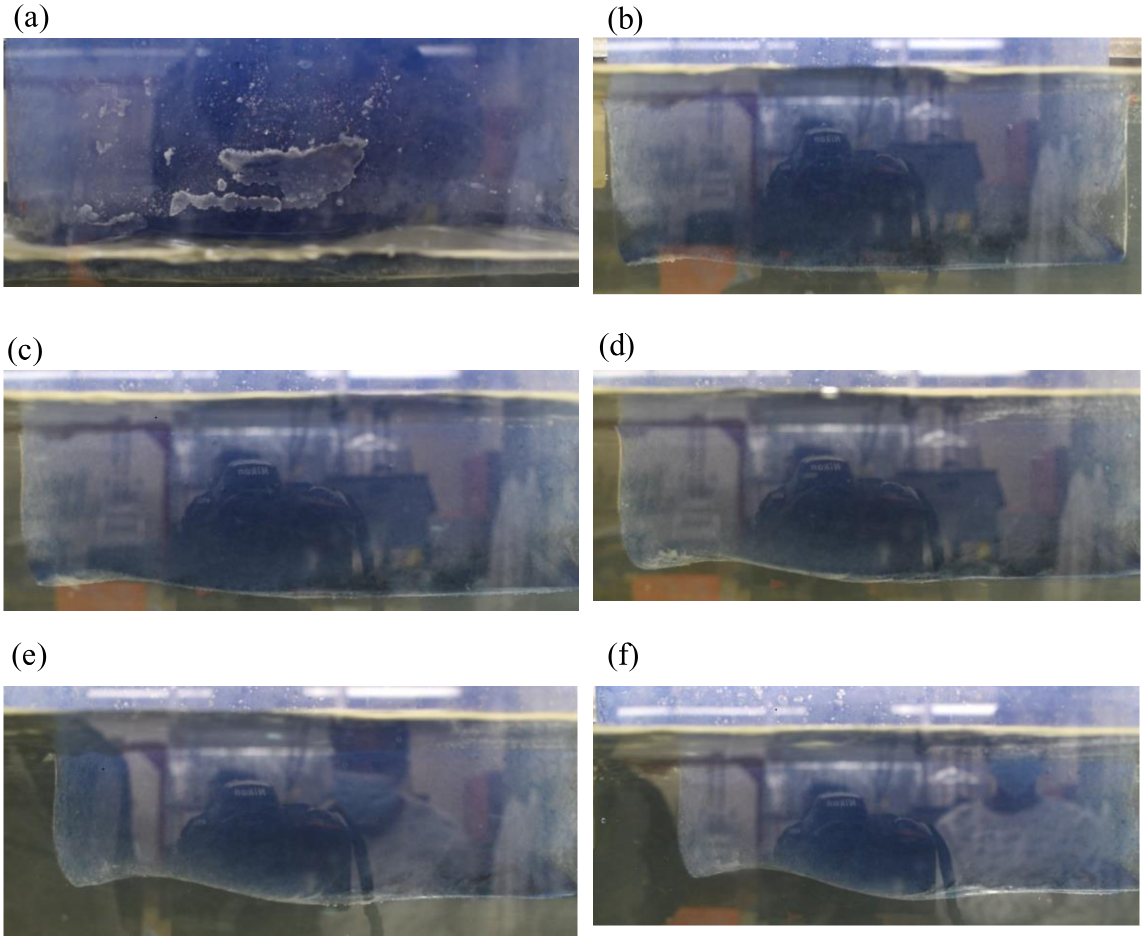

Figure 6.8: Time series of evolving ice (a) 0 minutes (b) 2 minutes (c) 4 minutes (d) 6 minutes (e) 8 minutes (f) 10 minutes

6.4 Discussion of Numerical Results

Commercial software was used to model and simulate the phenomenon with the solver changed to LES with the multiphase model flow technique. The simulation results in Figure 5.26 and 5.27 were validated using the linear-log plot in Figure 5.17. No data was observed in the viscous sublayer and buffer layer. As the Reynolds number increases, the data deviates from the logarithmic plot, leading to floating points beyond the computational domain.

Results from the enthalpy-porosity model presented scallops that are different in geometry from the ice scallops observed in the experimental approach. The enthalpy-porosity allowed only one material at a time, hence the inability to specify water as the primary material and ice as an additional material.

The flow of varying Reynolds numbers was evaluated, and the flow structure around the ice was modeled and simulated. Figures 5.21, 5.22, 5.23, and 5.24 show the streamwise velocity, vertical-velocity component, and pressure contour plots. From Figure 5.21, the maximum velocity was recorded for flow immediately surrounding the wake region. The maximum streamwise velocity is observed to increase with increasing Reynolds number. There is reverse flow observed at the point of flow separation and behind the block of ice. The recirculation of fluid contributes to the melting of the ice as the ice was exposed to the fluid for a longer period, contributing to the heat exchange at the ice-water surfaces before exiting. The vertical velocity component under the ice cover appears constant for the three Reynolds numbers and at a 0 – 0.1 m/s velocity. From the contour plots, the fluid separates as it encounters the ice and attaches along the surfaces of the ice, resulting in differential melting of the rectangular block of ice. The pressure contour plot shows that the pressure at the leading edge of the ice increases with increasing Reynolds number. The water hits the ice's surface perpendicular to the flow's direction, causing shearing at the ice-water interface. The magnitude of the frontal shearing depends on the Reynolds number. This observation complements the experimental results as the maximum melting occurs at the surface perpendicular to the flow, which increases with increasing Reynolds number. Downstream of the leading edge of the ice, there is a pressure drop and flow recirculation. Similarly, flow reversal is observed behind the block of ice and a subsequent decline in the pressure of the water.

Figure 6.9 shows the comparison of velocity profiles of different Reynolds numbers. At position x = -0.5 m from the graph, the velocity profiles for the three Reynolds numbers look similar despite the differences in fluid velocity. Re 32768 attained the highest speed of 0.2 m/s, followed by 0.19 m/s and 0.15 m/s for Re 30147 and Re 23265, respectively.

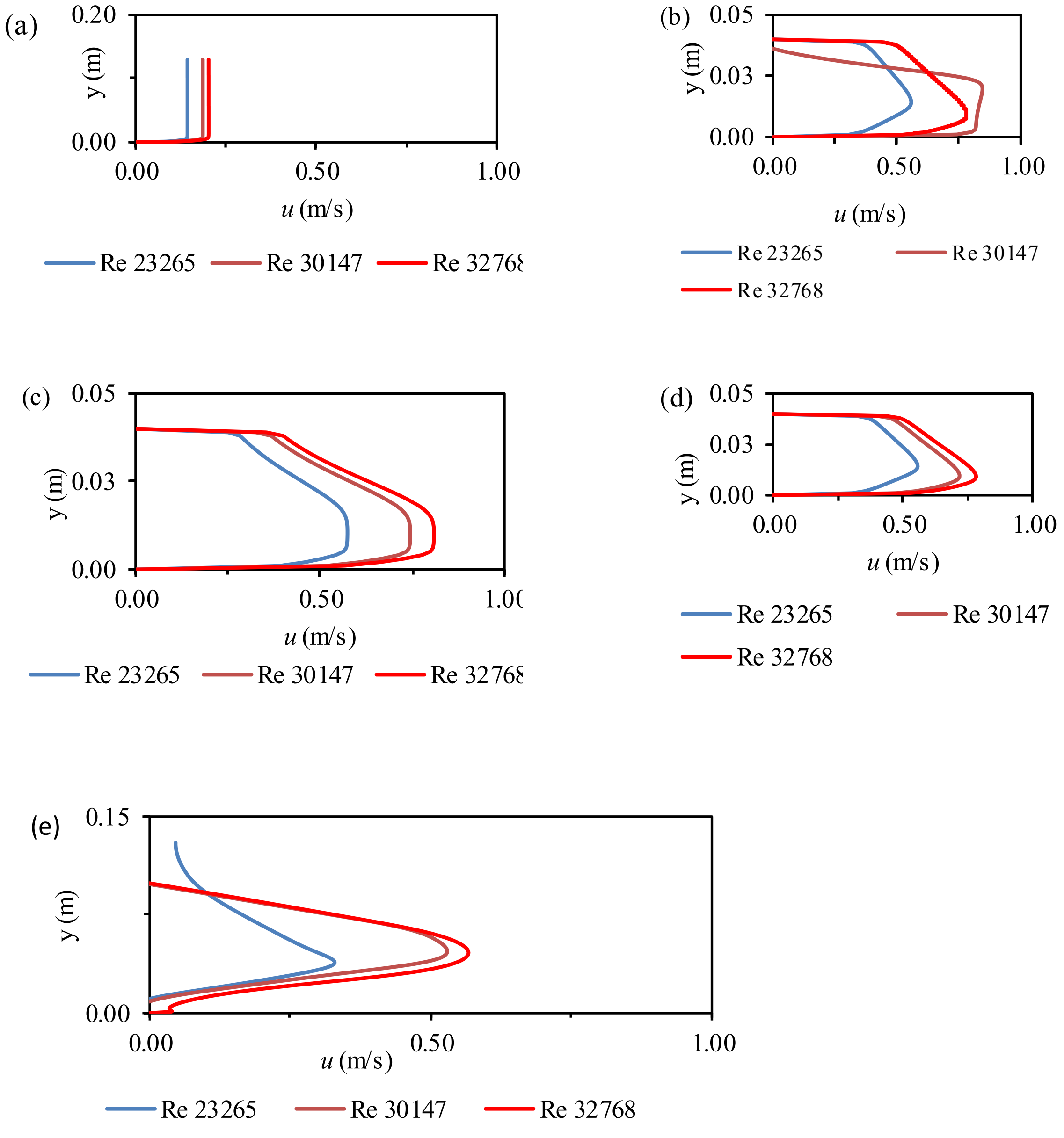

Figure 6.9: Comparison of velocity profiles for Re 23265, Re 30147 and Re 32768 at (a) *x* = -0.5 m (b) 0.1 m (c) 0.25m (d) 0.4 m (e) 0.8 m

At the rear end of the ice, the profiles look similar despite Re = 32768 attaining a maximum velocity of 0.81 m/s midspan of the channel. The velocities at the ice-water interface and the channel walls were 0 m/s. The velocity profiles at the rear end of the ice corresponding to x = 0.4 m have similar profiles at x = 0.25 m. However, the maximum velocity of the water recorded increases with increasing Reynolds number. Figure 6.9 (e) presents the profile at the rear end of the channel at x = 0.8 m. Flow reversal was observed close to the ice-water interface for Re = 32768 and Re = 30147. Meanwhile, flow reversal also occurred close to the channel walls in the three Reynolds numbers, according to the profiles. The shape of the profiles is due to the axial movement of the water as it exits the surfaces of the ice giving it the domed shape.

Chapter 7: Conclusion and Future Work

7.1 Conclusion

In this thesis, the mechanism for the formation of ice scallops for Reynolds numbers 2.3 x 10^4, 3.0 x 10^4 and 3.3 x10^4 were studied experimentally using a recirculation flow channel. The trend of results indicates an increase in the basal melt rate of ice with an increasing Reynolds number. As expected, it was observed that the surface perpendicular to the direction of the fluid flow experienced the maximum melt rate. It was observed that the maximum velocity occurred at the edge of the ice closest to the middle of the recirculation flume. For Re = 3.3 x 10^4 two scallops were formed on the ice block, and the measured wavelength of these scallops was 266 mm. For Re = 3.0 x 10^4 and 2.3 x 10^4 no visible additional scallop was formed at the tail of the samples. Temperature data from thermocouples frozen into the ice showed an increase in melt rate with increasing Reynolds number as reflected in the shorter times it took for thermocouples to reach the melting point when the flow corresponded to Re = 3.3 x 10^4 than for 3.0 x 10^4 and 2.3 x 10^4. These results indicated that the scallops formed due to turbulent structures and the separation and reattachment of fluid along the ice, giving rise to the non-uniform melting of the ice.

The numerical simulation showed the formation of scallops using the enthalpy-porosity approach. The numerical simulation showed that scallops are formed due to turbulence structures and the separation and reattachment of fluid along the ice, giving rise to the non-uniform melting of the ice.

7.2 Recommendations for Future Work

Based on the work carried out, the following are suggested:

1) Experimentally investigate the velocity profile along the scallop geometry to validate the numerical results.
2) Experimentally investigate the velocity profile along the scallop geometry to validate the numerical results and further enhance the understanding of ice scallop formation.
3) Improving data collection by incorporating a multi-data acquisition system for data accuracy and quality
4) Investigate the effect of ice grain size on the strength of ice samples and its associated impact on melting.

Through continued research in the field a deeper understanding of ice scallop formation processes and their effects on local ice loads can further reduce uncertainties in ice load modelling for engineering design.

Bibliography

A Palmer and K Croasdale (2012) Arctic offshore engineering. *World Scientific Publishing, Singapore*, 327pp. ISBN-10: 9-814368-77-6, ISBN-13: 978-9-814- 36877-3, hardback. 59(214), 393–393. http://doi.org/10.3189/2013JoG13J030

Bouzennada, T., Mechighel, F., Ghachem, K., & Kolsi, L. (2021). Numerical Simulation of the Impact of the Heat Source Position on Melting of a Nano-Enhanced Phase Change Material. Nanomaterials 2021, Vol. 11, Page 1425, 11(6), 1425. https://doi.org/10.3390/NANO11061425

Budwit-Hunter, C. (2015). *Ice Scour and Gouging Effects with Respect to Pipeline and Wellhead Final Report*.

Bushuk M, Holland, D. M., Stanton, T. P., Stern, A., & Gray, C. (2019a). Ice scallops: a laboratory investigation of the ice-water interface. *Journal of Fluid Mechanics*, *873*, 942–976. https://doi.org/10.1017/jfm.2019.398

Cenedese, C., & Straneo, F. (2022). *Annual Review of Fluid Mechanics Icebergs Melting*. https://doi.org/10.1146/annurev-fluid-032522

Chung, J. S., & International Society of Offshore and Polar Engineers. (2001). *The proceedings of the Eleventh (2001) International Offshore and Polar Engineering Conference : presented at: The Eleventh (2001) International Offshore and Polar Engineering Conference : held in Stavanger, Norway, June 17-22, 2001*. International Society of Offshore and Polar Engineers.

Claudin, P., Durán, O., & Andreotti, B. (2017). Dissolution instability and roughening transition. *Journal of Fluid Mechanics*, *832*, 832R21-832R214. https://doi.org/10.1017/jfm.2017.711

Croasdale, K., Brown, R., Campbell, P., Crocker, G., Jordaan, I., King, T., Mckenna, R., Myers, R., & Ottawa, C. (2001). Iceberg risk to seabed installations on the grand banks poac '0 1.

Darwish, M. S. (1993). A new high–resolution scheme based on the normalized variable formulation. Numerical Heat Transfer, Part B: Fundamentals, 24(3), 353–371. https://doi.org/10.1080/10407799308955898

Davison, B. J., Cowton, T. R., Cottier, F. R., & Sole, A. J. (2020). Iceberg melting substantially modifies oceanic heat flux towards a major Greenlandic tidewater glacier. *Nature Communications*, *11*(1). https://doi.org/10.1038/s41467-020-19805-7

Detert, J. R., Burris, E. R., Harrison, D. A., & Martin, S. R. (2013). Voice Flows to and around Leaders: Understanding When Units Are Helped or Hurt by Employee Voice. *Administrative Science Quarterly*, *58*(4), 624–668. https://doi.org/10.1177/0001839213510151

Ebrahimi, A., Kleijn, C. R., & Richardson, I. M. (2019). Sensitivity of numerical predictions to the permeability coefficient in simulations of melting and solidification using the enthalpy-porosity method. *Energies*, *12*(22). https://doi.org/10.3390/en12224360

Escudier, M. (2017). Turbulent flow. *Introduction to Engineering Fluid Mechanics*, 490–534. https://doi.org/10.1093/OSO/9780198719878.003.0018

Fequest, Dan., & Meteorological Service of Canada. (2005b). *MANICE : manual of standard procedures for observing and reporting ice conditions*. Environment Canada.

Iso (2019), Iso19906:2019 Petroleum and natural gas industries – Arctic offshore structures (2nd ed.) International organization for standardization

Ghidersa, B.-E. (2004). Finite volume-based volume-of-fluid method for the simulation of two-phase flows in small rectangular channels. https://www.researchgate.net/publication/34008099

Gilpin, R. R., Hirata, T., & Cheng, K. C. (1980). Wave formation and heat transfer at an ice-water interface in the presence of a turbulent flow. *Journal of Fluid Mechanics*, *99*(3), 619–640. https://doi.org/10.1017/S0022112080000791

Gualtieri, C., Angeloudis, A., Bombardelli, F., Jha, S., & Stoesser, T. (2017). On the values for the turbulent schmidt number in environmental flows. In *Fluids* (Vol. 2, Issue 2). MDPI AG.

https://doi.org/10.3390/fluids2020017

Hanratty, T. J. (1981). *stability of surfaces that are dissolving or being formed by convective diffusion*. www.annualreviews.org

Hester, E. W., McConnochie, C. D., Cenedese, C., Couston, L. A., & Vasil, G. (2021). Aspect ratio affects iceberg melting. Physical Review Fluids, 6(2). https://doi.org/10.1103/physrevfluids.6.023802

Iso (2019), ISO19906:2019 Petroleum and natural gas industries – Arctic offshore structures (2nd ed.). International Organization for Standardization

Ivanova, E. M., Noll, B. E., & Aigner, M. (2013). A numerical study on the turbulent schmidt numbers in a jet in crossflow. *Journal of Engineering for Gas Turbines and Power*, *135*(1). https://doi.org/10.1115/1.4007374

Jordaan, I. J. (2001). Mechanics of ice-structure interaction. www.elsevier.com/locate/engfracmech

Koide, Y., Kaithakkal, A. J., Schniewind, M., Ladewig, B. P., Stroh, A., & Friederich, P. (2021). *Machine learning for rapid discovery of laminar flow channel wall modifications that enhance heat transfer*. http://arxiv.org/abs/2101.08130

Koo, Y. H., Xie, H., Ackley, S. F., Mestas-Nuñez, A. M., Macdonald, G. J., & Hyun, C. U. (2021). Semi-automated tracking of iceberg B43 using Sentinel-1 SAR images via Google Earth Engine. *Cryosphere*, *15*(10), 4727–4744. https://doi.org/10.5194/TC-15-4727-2021

Launder, B. E. (2015). First steps in modelling turbulence and its origins: A commentary on Reynolds (1895) "On the dynamical theory of incompressible viscous fluids and the determination of the criterion." In *Philosophical Transactions of the Royal Society A: Mathematical, Physical and Engineering Sciences* (Vol. 373, Issue 2039). Royal Society of London. https://doi.org/10.1098/rsta.2014.0231

Little, C. M., Gnanadesikan, A., & Oppenheimer, M. (2009). How ice shelf morphology controls basal melting. *Journal of Geophysical Research: Oceans*, *114*(12).

https://doi.org/10.1029/2008JC005197

Maddux, T. B., Nelson, J. M., & McLean, S. R. (2003). Turbulent flow over three-dimensional dunes: 1. Free surface and flow response. *Journal of Geophysical Research: Earth Surface*, *108*(F1), n/a-n/a. https://doi.org/10.1029/2003jf000017

McGuire, P., Younan, A., Wang, Y., Bruce, J., Gandi, M., & King, T. (2016). *OTC-27473-MS Smart Iceberg Management System-Rapid Iceberg Profiling System.*

Ni, R., & Xia, K. Q. (2013). Kolmogorov constants for the second-order structure function and the energy spectrum. *Physical Review E - Statistical, Nonlinear, and Soft Matter Physics*, *87*(2). https://doi.org/10.1103/PhysRevE.87.023002

Niezgoda-Zelasko, B. (2016). The Enthalpy-porosity Method Applied to the Modelling of the Ice Slurry Melting Process during Tube Flow. *Procedia Engineering*, *157*, 114–121. https://doi.org/10.1016/j.proeng.2016.08.346

Pope, S. B. (2000). *Turbulent flows*. Cambridge University Press.

Presteau, X., Montreuil, E., Chazottes, A., Vancassel, X., & Personne, P. (2009). Experimental and numerical study of scallop ice on swept cylinder. *1st AIAA Atmospheric and Space Environments Conference*. https://doi.org/10.2514/6.2009-4124

Ramadhani, A., Khan, F., Colbourne, B., Ahmed, S., & Taleb-Berrouane, M. (2022). Resilience assessment of offshore structures subjected to ice load considering complex dependencies. *Reliability Engineering and System Safety*, *222*. https://doi.org/10.1016/j.ress.2022.108421

Ramudu, E., Hirsh, B. H., Olson, P., & Gnanadesikan, A. (2016). Turbulent heat exchange between water and ice at an evolving ice-water interface. *Journal of Fluid Mechanics*, *798*, 572–597. https://doi.org/10.1017/jfm.2016.321

Richardson, K., Carling, Paul., & Geological Society of America. (2005). *A typology of sculpted forms in open bedrock channels*. Geological Society of America.

Riglin, J., & Reid, B. (2021a). Applied Computational Fluid Dynamics and Turbulence Modeling. *59*(5), 1891–1892. https://doi.org/10.2514/1.J060595

Rolfo, S. (2010). les and hybrid rans/les turbulence modelling in unstructured finite volume code and applications to nuclear reactor fuel bundles.

Schmitt, F. G. (2007). About Boussinesq's turbulent viscosity hypothesis: historical remarks and a direct evaluation of its validity. In *Comptes Rendus - Mecanique* (Vol. 335, Issues 9–10, pp. 617–627). https://doi.org/10.1016/j.crme.2007.08.004

Shi, J., Thomas, T. G., & Williams, J. J. R. (1999). Large-eddy simulation of flow in a rectangular open channel. Journal of Hydraulic Research, 37(3), 345–361. https://doi.org/10.1080/00221686.1999.9628252

Stoesser, T., Rodi, W., & Fröhlich, J. (2005). *large eddy simulation of open-channel flow over a layer of spheres*.

Tang, H., Lei, Y., Li, X., & Fu, Y. (2019). Large-eddy simulation of an asymmetric plane diffuser: Comparison of different subgrid scale models. Symmetry, 11(11). https://doi.org/10.3390/sym11111337

Taylor, J. R., Sarkar, S., & Armenio, V. (2005a). Large eddy simulation of stably stratified open channel flow. *Physics of Fluids*, *17*(11), 1–18. https://doi.org/10.1063/1.2130747

Tominaga, A., & Nezu, I. (1991). Turbulent Structure in Compound Open Channel Flows. Journal of Hydraulic Engineering, 117(1), 21–41. https://doi.org/10.1061/(ASCE)0733-9429(1991)117:1(21)

van Leer, B., & Powell, K. G. (2010). Introduction to Computational Fluid Dynamics. In Encyclopedia of Aerospace Engineering. John Wiley & Sons, Ltd. https://doi.org/10.1002/9780470686652.eae048

Virag, Z., Živić, M., & Galović, A. (2006). Influence of natural convection on the melting of ice block surrounded by water on all sides. *International Journal of Heat and Mass Transfer*, *49*(21–22), 4106–4115. https://doi.org/10.1016/j.ijheatmasstransfer.2006.04.007

Voller, V. R., Swaminathan, C. R., & Thomas, B. G. (1990). fixed grid techniques for phase change problems: a review. in *international journal for numerical methods in engineering* (Vol. 30).

W Wagner, T. J., Dell, R. W., & Eisenman, I. (2017). An Analytical Model of Iceberg Drift. https://doi.org/10.1175/JPO-D-16-0262.s1

Xie, Z., Associate, R., Binliang, L., Falconer, R. A., & Maddux, T. B. (2014). Large-eddy simulation of turbulent open-channel flow over three-dimensional dunes.